

# Structural analysis of disk super star clusters of M82: size and profile shape at intermediate ages

B. Cuevas-Otahola,<sup>1\*</sup> Y. D. Mayya,<sup>1</sup> I. Puerari<sup>1</sup> and D. Rosa-González<sup>1</sup>

<sup>1</sup>*Instituto Nacional de Astrofísica, Óptica y Electrónica, 72840 Puebla, Mexico*

Accepted XXX. Received YYY; in original form ZZZ

## ABSTRACT

We present the structural parameters of 99 Super Star Clusters (SSCs) in the Disk of M82. Moffat-EFF, King and Wilson models were fitted using a  $\chi^2$  minimisation method to background-subtracted Surface Brightness Profiles (SBPs) in F435W (B), F555W (V), and F814W (I) bands of the Advanced Camera for Surveys (ACS) of the Hubble Space Telescope (HST). The majority of the SSC profiles is best-fitted by the Moffat-EFF profile. The scale parameter  $r_d$  and the shape parameter  $\gamma$  in the three filters are identical within the measurement errors. The analysed sample is big enough to allow characterisation of the distributions of core radii  $R_c$  and  $\gamma$ . The obtained distribution of  $R_c$  follows a log-normal form, with center and  $\sigma \log(\frac{R_c}{pc})$  being 1.73 pc and 0.25, respectively. The  $\gamma$  distribution is also log-normal with center and  $\sigma \log(\gamma)$  being 2.88 and 0.08, respectively. M82 is well-known for the absence of current star formation in its disk, with all disk SSCs older than 50 Myr and hardly any cluster older than  $\sim 300$  Myr. The derived distributions compare very well with the distributions for intermediate-age clusters in the Large Magellanic Cloud (LMC), which is also a low-mass late-type galaxy similar to M82. On the other hand, the distributions of  $R_c$  in both these galaxies are shifted towards larger values as compared to SSCs of similar age in the giant spiral galaxy M83. M82 and LMC also span a narrower range of  $\gamma$  values as compared to that in M83.

**Key words:** galaxies: clusters: general – (Galaxy:) globular clusters: general – catalogues

## 1 INTRODUCTION

Understanding the formation and evolution of globular clusters (GCs) has been an active field of research in astrophysics over the last half century (Forbes et al. 2018). The discovery of clusters as dense ( $\rho \gtrsim 10^3 M_\odot/pc^3$ ) and massive ( $10^4 - 10^6 M_\odot$ ) as GCs, but relatively young, known as Young Massive Clusters or Super Star Clusters (SSCs), has given a new impetus to these studies in the last two decades (Bastian 2016). SSCs are often thought to be the progenitors of GCs, and hence their study has the potential to throw light on the processes that the GCs may have experienced during their early evolution (Portegies Zwart et al. 2010). SSCs are subjected to different physical processes at different timescales: at short ( $\lesssim 10^7$  yr) and intermediate timescales ( $10^7 - 10^8$  yr), stellar evolutionary processes (stellar winds, supernovae, etc) play a role; at later times ( $\gtrsim 10^8$  yr) dynamical processes start becoming important: the most dominant of them being the gravitational shocks

due to the interaction of the cluster with the tidal field of its host galaxy, and two-body relaxation (Spitzer 1987). These processes increase the velocity of some stars above the escape velocity, forcing them to leave the cluster, resulting in the dissipation and/or complete disruption of the cluster. The selective loss of high-velocity stars from the central regions of the clusters leads to collapse of the core at late times (Lynden-Bell et al. 1968). The extent to which a cluster is subjected to these effects depends on its 3-dimensional location in its host galaxy, galacto-centric distance, in addition to the gravitational potential field of the host galaxy itself (Fall & Zhang 2001). Besides, clusters located in the disk suffer from encounters with Giant Molecular Clouds when they pass through the spiral arms (Gieles et al. 2006). Mackey et al. (2008) analysed the effect of binary and single black holes and found them to be responsible of expansion of the core at times  $\gtrsim 600$  Myr in clusters in the Large Magellanic Clouds (LMC). In the presence of a tidal field, the sizes of the expanding clusters would be limited to their tidal radius (Gieles 2013).

The structure of star clusters has been modelled the-

\* E-mail: bolivia@inaoep.mx

oretically using auto-gravitating isothermal spheres of lowered kinetic energy in the presence of external tidal forces. These configurations, usually known as King models following the classical treatment of [King \(1966\)](#), explain satisfactorily the observed surface brightness profiles (SBPs) of old stellar systems such as GCs ([Baumgardt & Hilker 2018](#)). The most salient feature of these SBPs is the existence of a core-halo structure, with the core characterised by the core radius and the halo limited by the tidal radius. On the other hand, SBPs of slightly younger systems such as the blue population of clusters in the LMC, lack core-halo structure and instead follow power-law forms. [Elson et al. \(1987\)](#) found that these SBPs are well-represented by Moffat profiles (Moffat-EFF profiles, henceforth). The profile of the most massive and luminous SSC in the LMC, R136, is also consistent with a Moffat-EFF profile ([Elson et al. 1992](#)). [Mackey & Gilmore \(2003a\)](#) fitted Moffat-EFF profiles to the SBPs of 53 star clusters in the LMC to obtain their structural parameters. Wilson profiles, originally proposed by [Wilson \(1975\)](#) to characterise SBPs of elliptical galaxies, are also found to be good fits to the SBPs of SSCs in the LMC ([McLaughlin & van der Marel 2005](#)). The power-law nature of SBPs at relatively younger ages is understood to be due to the contribution of stars in the unbound halo ([Elson et al. 1987](#); [Moreno et al. 2014](#)).

Hubble Space Telescope (HST), especially the wide field of the Advanced Camera for Surveys (ACS), has enabled the detection of large populations of SSCs in external galaxies, some examples being M82 ([O’Connell et al. 1995](#); [Melo et al. 2005](#); [Mayya et al. 2008](#)), M51 ([Chandar et al. 2011](#)), M81 ([Chandar et al. 2001](#); [Santiago-Cortés et al. 2010](#)), M83 ([Bastian et al. 2011](#); [Ryon et al. 2015](#)), and Antennae (NGC4038/4039) ([Whitmore & Schweizer 1995](#)). Clusters have been reported in 20 other nearby spiral and irregular galaxies using the Hubble Legacy Archive (HLA) data ([Whitmore et al. 2016](#)).

Modern  $\chi^2$  minimisation technique allows the analysis of the SBPs of SSCs with empirical formulae in an objective way. Moffat-EFF and empirical formulae for King models ([King 1962](#)), available directly in profile analysing tools such as ISHAPE ([Larsen 1999](#)) and GALFIT ([Peng et al. 2010](#)), are the most often used profiles for fitting SBPs of SSCs. The output parameters commonly obtained by such analysis are core radius and half-light radius, often for an assumed form of the profile shape (e.g. [Bastian et al. 2008](#)). [Ryon et al. \(2015\)](#) and [Ryon et al. \(2017\)](#) carried out the analysis of structural parameters on the HST images of  $\sim 700$  Young Massive Clusters (YMCs) in the giant spiral M83, and in two late-type galaxies (NGC 628 and NGC 1313). They obtained core radius, half-light radius, and the shape parameters using Moffat-EFF profile in GALFIT for 478 YMCs that are well resolved on the HST images. For the rest of the YMCs, they obtained half-light radius based on an empirical relation between the concentration index, defined as the difference in magnitudes between 1 and 3 pixel radius apertures, and half-light radius on mock YMCs. YMCs they analysed are in general younger than 1 Gyr, and constitute the largest sample of intermediate-age YMCs with uniformly determined structural parameters.

[McLaughlin & van der Marel \(2005\)](#) proposed an alternative technique to obtain structural parameters of star clusters. Their method involves fitting the observed profiles

directly with the profiles generated using dynamical models that have underlying physical basis such as [King \(1966\)](#) and [Wilson \(1975\)](#). They also suggested using Jeans theorem to construct dynamical models that are consistent with the empirical Moffat-EFF profile. They used this technique to obtain a complete set of dynamical parameters, not just core radius and half-light radius, for GCs in the Milky Way and Fornax galaxies, and blue and red star clusters in the SMC and LMC galaxies. The technique has been recently extended by [Sollima et al. \(2015\)](#) to implement anisotropic King-Michie models. For clusters of known age, and hence known photometric masses, this technique is able to extract the central and line-of-sight velocity dispersions. The latter parameter could be determined observationally using high spectral resolution observations, which allows a direct verification of the validity of the assumption of the dynamical models used. The HST images of galaxies that are nearer than  $\sim 5$  Mpc have sufficient spatial resolution (1 pix=1.25 pc at 5 Mpc) for the construction of SBPs good enough not only for the determination of their sizes, but also for a detailed analysis using dynamical models. Beyond the Milky Way, M31 and NGC5128 are the only two giant galaxies where SSC profiles have been analysed using dynamical models ([Barmby et al. 2007](#); [McLaughlin et al. 2008](#); [Wang & Ma 2013](#)).

M82 is an excellent candidate to carry out such a study, as it is relatively nearby (3.63 Mpc [Freedman et al. 1994](#)), and has a rich population of clusters in its nucleus and disk ([Mayya et al. 2008](#)). Spectroscopic ages have been obtained for around 40 of the disk SSCs. The derived ages occupy a relatively narrow range between 50–300 Myr ([Konstantopoulos et al. 2009](#)). [Mayya et al. \(2006\)](#) suggested, based on the analysis of the photometric, dynamical, and chemical properties, that the entire galaxy participated in a disk-wide burst of duration of a few hundred million years. The disk stopped forming stars around 50 Myr ago, which is well supported by the absence of red supergiants in its disk ([Davidge 2008](#)). The disk-wide burst, and the formation of disk clusters, were most likely triggered by the interaction of M82 with its neighbours M81 and NGC 3077 ([Yun 1999](#)). The narrow age range of disk SSCs is consistent with them being formed in the disk-wide burst. The existence of a few hundreds of massive SSCs, all of ages intermediate between the YMCs and the old GCs, gives us a great opportunity to understand the dynamical effects experienced by evolving clusters.

In §2, we summarise the general properties of the sample of SSCs in the disk of M82, as well as the procedure followed in this work to obtain the background-subtracted SBPs. In §3, we describe the SBPs expected in theoretical models such as King and Wilson, and empirical formulae (Moffat-EFF), as well as the procedure followed to obtain the structural parameters from the observed SBPs. Model-derived parameters are presented and their statistical properties discussed in §4. The results are summarised in §5.

## 2 M82 SSC SAMPLE AND EXTRACTION OF SURFACE BRIGHTNESS PROFILES

The sample of SSCs for structural analysis was selected from the catalogue of M82 disk SSCs from [Mayya et al. \(2008\)](#),

**Table 1.** Fitting radius and background value for all M82 disk SSCs

| ID <sup>†</sup> | R.A.<br>(deg) | DEC<br>(deg) | $R_{\text{ip}}$<br>(pix) | $R_{3\sigma}$<br>(pix) | $\mu_{\text{bg}} \pm \delta\mu$<br>(mag/arcsec <sup>2</sup> ) |
|-----------------|---------------|--------------|--------------------------|------------------------|---|
| (1)             | (2)           | (3)          | (4)                      | (5)                    | (6)   |
| D1              | 148.94615     | 69.67842     | 19                       | 23                     | 18.42±0.22  |
| D2              | 149.00384     | 69.68513     | 14                       | 24                     | 18.20±0.30  |
| D3              | 149.01420     | 69.68672     | 18                       | 50                     | 18.89±0.44  |
| D4              | 148.94655     | 69.67856     | 9                        | 26                     | 18.48±0.22  |
| D5              | 148.94480     | 69.67737     | 11                       | 16                     | 19.11±0.32  |
| D6              | 149.00952     | 69.68584     | 18                       | 34                     | 18.74±0.32  |
| D7              | 149.00372     | 69.68566     | 11                       | 14                     | 17.84±0.17  |
| D8              | 149.05942     | 69.69909     | 25                       | 26                     | 20.34±0.12  |
| D9              | 148.98191     | 69.68497     | 14                       | 34                     | 19.02±0.21  |
| D10             | 148.98767     | 69.68537     | 9                        | 28                     | 18.88±0.16  |

<sup>†</sup>IDs from Mayya et al. (2008). The 'D' preceding the numbers stands for 'disk' sample

which consists of 393 objects, and is based on the detection of SSCs in F435W (B), F555W (V) and F814W (I) bands of the HST/ACS. The entire sample is presented in Table 3 of Mayya et al. (2008). In §2.2, we will compare the magnitude and colour properties of the subsample with respect to the entire sample.

## 2.1 Surface brightness profiles

We used the same images which were used for cluster detection to extract SBPs. These images were part of the HST Legacy Survey, which were made available in reduced form by the Hubble Heritage Team (Mutchler et al. 2007). The image scale corresponds to  $0.05'' \text{ pixel}^{-1}$  and covers the entire optical extent of M82. Exposure times were 1600, 1360 and 1360 seconds in filters B, V and I, respectively. The zero-point magnitudes in the Vega system were extracted from Sirianni et al. (2005), with values 25.779, 25.724, and 25.501 for B, V, and I bands, respectively.

Profile fitting packages such as GALFIT and ISHAPE analyse 2-dimensional (2-D) images to obtain structural parameters of star clusters. On the other hand, azimuthally averaged 1-dimensional (1-D) profiles have been used traditionally to obtain structural parameters of well-resolved clusters in the Milky Way and local group galaxies (e.g. Elson et al. 1987; McLaughlin & van der Marel 2005). The profile functions used in both these techniques are 1-D profiles applicable to spherically symmetric 3-D models. Moreover, derived structural parameters such as core radius and half-light radius refer to the radially symmetric configurations. We hence adopt the 1-D technique in this study. The *ellipse* task (Jedrzejewski 1987) in IRAF/STSDAS package is the standard tool to obtain the azimuthally averaged 1-D profiles of extended objects. Though the task is developed for analysing the surface brightness profiles of external galaxies, the task does an excellent job in obtaining 1-D SBPs of clusters on the HST images. We fixed the centers of the ellipses at the centroids of the SSCs, and obtained the SBPs at successive HST/ACS pixels, with a width of 1 pixel (0.88 pc at the distance of M82). The task also calculates the azimuthal dispersions in the intensity at each

radial bin, which is a measure of errors in the SBPs. We left the ellipticity ( $\epsilon = 1 - b/a$ , where  $a$  and  $b$  are semi-major and semi-minor axes, respectively) and position angle as free parameters in a first run of the task. The distribution of ellipticities peaks at 0.19 with only 25% of the SSCs having higher ellipticities. This is illustrated in Fig. A1 of the Appendix. Thus, the majority of the SSCs are nearly circular. With  $\epsilon = 0.3$ , the well-known SSC M82-F (D1) is one of the most elongated clusters. The SBP obtained for this cluster using circular and elliptical ( $\epsilon = 0.30$ ) apertures are similar (see Fig. A2 in the Appendix). Smith & Gallagher (2001) also found that the half-light radius obtained from profiles using circular and elliptical apertures for M82-F are similar, which confirms that the derived structural parameters are not very sensitive to small differences in ellipticities. We hence fixed the ellipticity at the minimum value permitted by the task, which is  $\epsilon = 0.05$ .

The surface brightness profiles obtained by the *ellipse* task contain background contribution which should be subtracted in order to obtain pure cluster profiles. This background in the case of M82 clusters mainly comes from its disk, which varies appreciably from one cluster to another. This makes the measurement of background for each cluster mandatory. We analysed the four corners of the cut-outs for finding an appropriate local background value for each SSC. Median and standard deviation values were obtained in boxes of  $10 \times 10$  pixel size at the four corners of the cut-out images, the minimum of these four values being chosen as the background  $I_{\text{bg}}$  and the noise  $\sigma_{\text{bg}}$  respectively. For each background-subtracted profile, we determined a limiting radius, defined as the outer-most point of the profile at which the cluster surface brightness is equal to 3 times  $\sigma_{\text{bg}}$ . We refer to this radius as  $R_{3\sigma}$ .

Cluster SBPs are expected to monotonically decrease up to  $R_{3\sigma}$ . However, we found that the majority of the profiles have an inflexion point at  $R < R_{3\sigma}$ . Visual examination of the images suggested that this is due to stars or clusters in the neighbourhood of the object of analysis. When possible, we masked the contaminating sources in each cut-out image before obtaining SBPs. In a few cases, the masks were successful in producing SBPs free from contamination from neighbours. However, in the majority of the cases, SBPs are affected due to some residual contribution from the neighbours. This is because in most of the cases the contaminating source is another SSC, which occupies a non-negligible number of pixels of the cut-out image. We took into account this effect by defining a fitting radius for each SSC, within which the profile is free from contamination from a neighbour. We obtained this radius by determining the innermost inflexion point  $R_{\text{ip}}$ , such that at  $R_{\text{ip}}$ ,  $\frac{d^2 I}{dR^2} = 0$ , for each background-subtracted profile. In general, the fitting radius,  $R_{\text{fit}}$ , is the minimum of  $R_{\text{ip}}$  and  $R_{3\sigma}$ . However in all cases  $R_{\text{ip}} < R_{3\sigma}$ , and hence,  $R_{\text{fit}} = R_{\text{ip}}$ .

The profile analysis was carried out in the BVI HST/ACS bands. In each of these bands, the above procedure is repeated. Hence, we have a set of  $I_{\text{bg}}$ ,  $\sigma_{\text{bg}}$ ,  $R_{\text{ip}}$ ,  $R_{3\sigma}$ , and  $R_{\text{fit}}$  for each band.

In Figure 1, we illustrate the procedure adopted for obtaining the fitting radius for two clusters, one unaffected by a contaminating object (D8) and the other with a bright nearby contaminating source (D4). In the former case,  $R_{\text{ip}}$  is almost equal to  $R_{3\sigma}$ , whereas in the latter case,  $R_{\text{ip}}$  is less

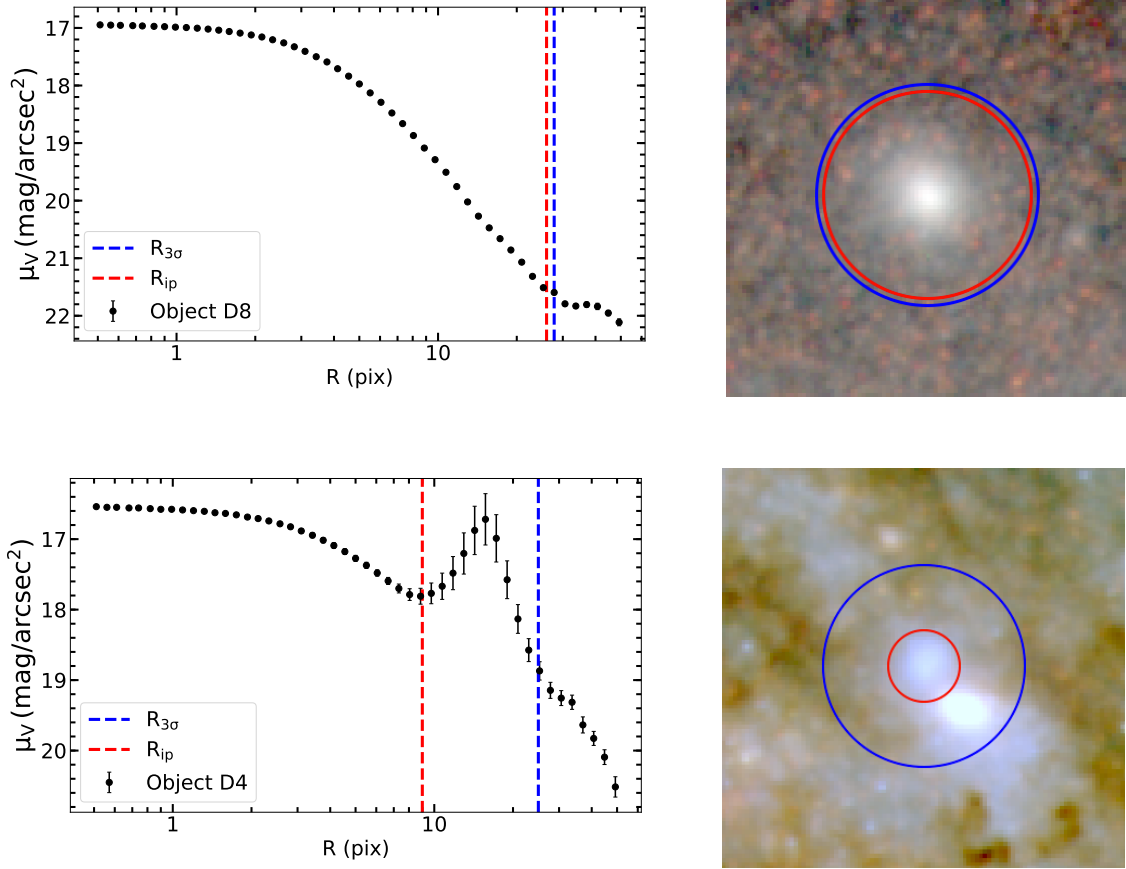


**Figure 1.** The  $V$ -band surface brightness profiles (left) and RGB image, constructed from  $I$  ( $R$ ),  $V$  ( $G$ ) and  $B$  ( $B$ ) bands (right) of two clusters, illustrating the procedure adopted for selecting the fitting radius. In the top, we illustrate it for the SSC D8, an isolated cluster, whereas in the bottom, we illustrate it for a highly-contaminated, but still useful, SSC D4. The  $R_{3\sigma}$ , the radius where the background-subtracted intensity is  $3 \times \sigma_{bg}$ , and  $R_{ip}$ , the inflexion radius where  $\frac{d^2 I}{dR^2} = 0$  are shown by vertical dashed lines (left) and circles (right) of blue and red colours, respectively. Note that the profiles are shown with logarithmic steps to illustrate the inner and outer profile shapes, simultaneously.

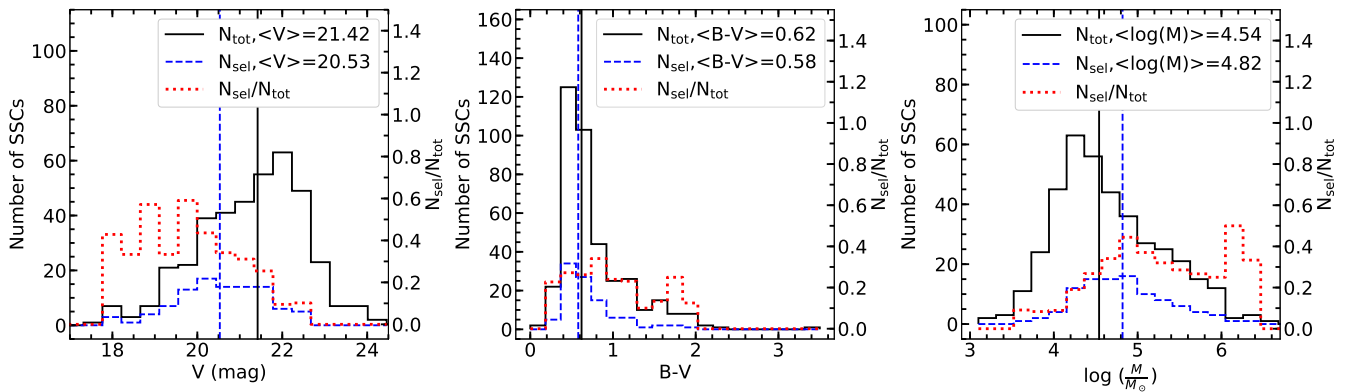


**Figure 2.** Comparison of distributions of  $V$  Magnitude (left),  $B - V$  (middle) and Cluster mass (right) of all M82 disk SSCs (black solid line) with the selected sample (99 clusters) (blue dashed line). Median values of the distributions are shown by the vertical lines and written in the top-right corner. The fraction of objects ( $N_{sel}/N_{tot}$ ) in each bin is shown by a red dotted line.

than half of  $R_{3\sigma}$ . The bump immediately beyond  $R_{\text{ip}}$  is due to the contaminating object, which can be seen in the RGB image. In Table 1, we give the values of  $R_{\text{fit}}$ ,  $R_{3\sigma}$  and the background surface brightness ( $\mu$ ) and its error ( $\delta\mu$ ), as well as the R.A. and DEC for all SSCs. The error is calculated as  $\delta\mu = 1.086 \left( \frac{\sigma_{\text{bg}}}{I_{\text{bg}}} \right)$ .  $R_{\text{fit}}$  in all cases is the inflexion radius  $R_{\text{ip}}$ .

In the following subsection, we will discuss the global properties of the selected 99 SSCs with respect to the total SSCs disk sample.

## 2.2 Selection and characteristics of the disk subsample

In order to obtain reliable structural parameters from the HST images, star clusters have to satisfy certain criteria. The most important of these criteria is that they have enough number of pixels for profile analysis. In the absence of a contaminating source, the number of pixels for analysis depends on the intrinsic size of the cluster. Another criterion for selection of clusters is that the extracted profile is well-fit by one of our models, quantified by  $\chi^2$  statistics, and described in the next section. We carried out an analysis of synthetic clusters in order to define the  $R_{\text{fit}}$  necessary to reliably recover the input parameters, which is also described in the next section. Based on this analysis, we considered a cluster to be good for analysis (1) if the  $R_{\text{fit}} \geq 8$  pixels in at least two bands and (2) the  $\chi^2$  of the best fit is less than  $3 \times \nu$ , where  $\nu$  is the number of degrees of freedom (Avni 1976; Wall & Jenkins 2003) (criterion 1 and 2, respectively). In the majority of the cases, B and V bands have similar behaviour with the I band displaying a different behaviour, with  $\sim 16\%$  having less than 8 pixels in I. The imposition of this criterion reduced our sample size to a subsample of 99 SSCs.

In order to determine how representative is the subsample with respect to the total sample, we compare the distributions of three of the most important characteristics for the two samples in Fig 2. The chosen characteristics are: V magnitude, B–V colour and the photometric mass. Given that most of the disk SSCs are formed in a disk-wide burst around 300 Myr ago, little dispersion is expected in the intrinsic colours and mass-to-light ratios of the SSCs. However, M82 SSCs suffer from considerable extinction, which gives rise to large dispersion in their colours. In this work, we assume that the entire dispersion in the colour histogram is caused by reddening. Hence, extinction-corrected magnitude is directly a measure of the mass for these SSCs. Our subsample contains between 20–40% of the total sample for B–V=0.2–2.0 mag, V=18–22 mag, and  $\log M/M_{\odot}$ =4.5–6.5 dex. In summary, our subsample represents the bright (V>18.0 mag), massive ( $M > 3 \times 10^4 M_{\odot}$ ) end of the total sample of SSCs, covering uniformly the entire range of extinction values. This subsample is complete above mass of  $M > 3 \times 10^4 M_{\odot}$ , which is very close to the turn-over in the mass function for the entire cluster sample (Mayya et al. 2008). Thus, our subsample is representative of the massive end of the luminosity function.

## 3 DETERMINATION OF STRUCTURAL PARAMETERS

Structural parameters were obtained by fitting the observed SBPs with PSF-convolved theoretical profiles. The fitted model profiles are Moffat-EFF (Elson et al. 1987), King (King 1966), and Wilson (Wilson 1975). We followed the procedure described in detail in McLaughlin & van der Marel (2005), which we summarise briefly in this section.

### 3.1 Dynamical models of star clusters

King and Wilson models are based on a “lowered” Maxwellian kinetic energy distribution function of stars. These two model structures differ only in the outer halo regions, which is due to an extra term in the Wilson formulation and are defined in terms of the distribution function of a relative energy  $\mathcal{E} = -E + \Phi_0$ , where  $E$  is the total energy for a star moving with an isotropic velocity  $v$  under a potential  $\Phi$ . The term  $\Phi_0$  is a constant such that the relative energy is positive everywhere in the cluster. Under this formulation, the relative potential  $\Psi = -\Phi + \Phi_0$  and  $\mathcal{E} = \Psi - \frac{1}{2}v^2$ . The models described above are given by:

$$\text{King : } f(\mathcal{E}) \propto \begin{cases} e^{(\mathcal{E}/\sigma_0^2)} - 1, & \mathcal{E} > 0, \\ 0, & \mathcal{E} \leq 0, \end{cases}, \quad (2)$$

$$\text{Wilson : } f(\mathcal{E}) \propto \begin{cases} e^{(\mathcal{E}/\sigma_0^2)} - 1 - \frac{\mathcal{E}}{\sigma_0^2}, & \mathcal{E} > 0, \\ 0, & \mathcal{E} \leq 0, \end{cases}, \quad (3)$$

where  $\sigma_0$  is a scale parameter which measures the core dispersion velocity defined as:

$$\sigma_0^2 \equiv \frac{4\pi G \rho_0 r_0^2}{9}, \quad (4)$$

where  $\rho_0$  is the central stellar density and  $r_0$  the scale radius, commonly referred to as King radius. These models are parametrised by a dimensionless potential  $W = \Psi/\sigma_0^2$ , which is defined at all radii inside the tidal radius  $r_t$ , and has the boundary values of  $W(r=0) \equiv W_0$  and  $W(r=r_t) = 0$ .  $W_0$  is a measure of the central potential, being directly related to the often-used concentration parameter  $c = \log(\frac{r_t}{r_0})$ . In this work, we varied the  $W_0$  values between 2 and 15, which corresponds to  $c = 0.5$  and 3.3 for King models and  $c = 0.7$  and 4.1 for Wilson models.

The solution of these equations is expressed as a function of  $W(r)$ , which is directly related to the 3-D density function,  $\rho(r)$  through the Poisson equation (as well as a normalised velocity dispersion profile, in terms of the central velocity dispersion, solving Jeans Equation). The observable quantity  $I(R)$  is obtained from  $\rho(r)$  by projecting it into the plane of the sky along the  $R$  axis following the standard formulation (e.g. Eq. 2.138a in Binney & Tremaine 1987) and dividing by the mass-to-light ratio  $\Gamma$ :

$$I(R) = \frac{\Sigma(R)}{\Gamma} = \frac{2}{\Gamma} \int_R^{R_t} \frac{\rho(r)}{(r^2 - R^2)^{\frac{1}{2}}} r dr, \quad (5)$$

where the integration limits are defined as  $R = r/r_0$  and  $R_t = r_t/r_0$ ,  $r_0$  being obtained by fitting model profiles to

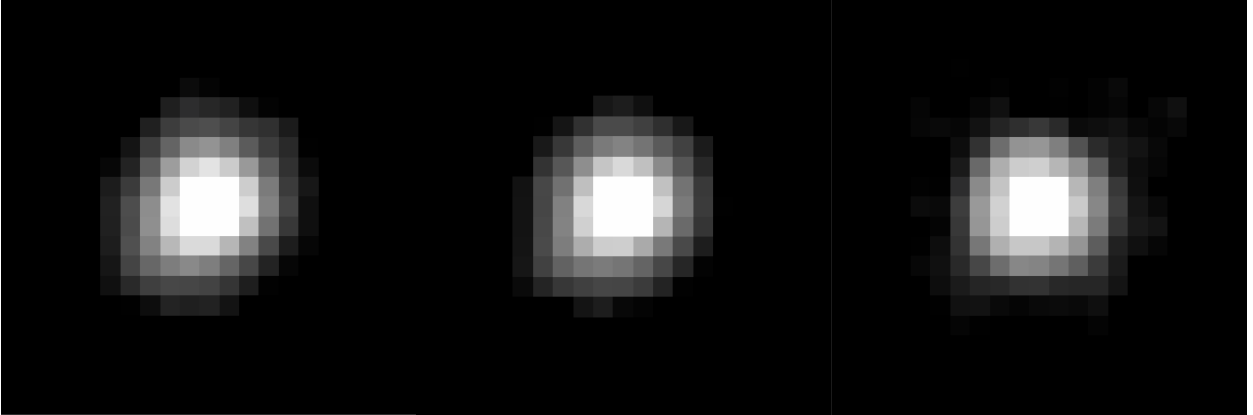


**Figure 3.** PSF images in B (left), V (middle) and I (right) bands calculated using PSFex (Bertin 2011).

observed SBPs. The cluster extends up to the tidal radius  $r_t$ , where by definition  $E = 0$ .

The Moffat-EFF profiles were proposed by Elson et al. (1987) as a convenient modification of the empirical King profile (King 1962) to fit the SBPs of LMC clusters. The functional form of the profile is:

$$I(R) = \frac{(\gamma - 2)L_{\text{tot}}}{2\pi r_d^2} \left[ 1 + \left( \frac{R}{r_d} \right)^2 \right]^{-\gamma/2}, \quad (6)$$

where  $R$  is the semi-major axis of the observed profile,  $r_d$  is the characteristic radius which is related to the core radius,  $R_c$  by:

$$r_d = \frac{R_c}{(2^{2/\gamma} - 1)^{1/2}} \quad (7)$$

Once  $\gamma$  and  $r_d$  are determined from the fitting, the 3-D luminosity density profile can be calculated using the expression:

$$j(r) = j_0 \left( 1 + \frac{r^2}{r_d^2} \right)^{-(\gamma+1)/2}, \quad (8)$$

The mass density is obtained using  $\rho(r) = \Gamma j(r)$ . On the other hand, a velocity profile is found solving Poisson and Spherical Jeans equations, giving rise to a normalised velocity dispersion profile in terms of the central velocity dispersion  $\sigma_0$ . The surface mass-density  $\Sigma$  is found by projecting the volume mass density  $\rho(r)$  into the plane of the sky, following Eq. 5. The surface density profile also allows us to calculate numerically  $R_h$ , the radius containing half the total light.

### 3.2 PSFs

Intrinsic cluster profiles are broadened due to the PSF of the instrument, and hence in order to determine the structural parameters, especially the core parameter, it is essential to convolve the model profiles with the instrumental PSF profiles before comparing with observed SBPs. We used the PSFex (Bertin 2011) tool to obtain a PSF in each of the three bands. Before using this tool, we selected a list of suitable stars in each of these bands using SExtractor (Bertin

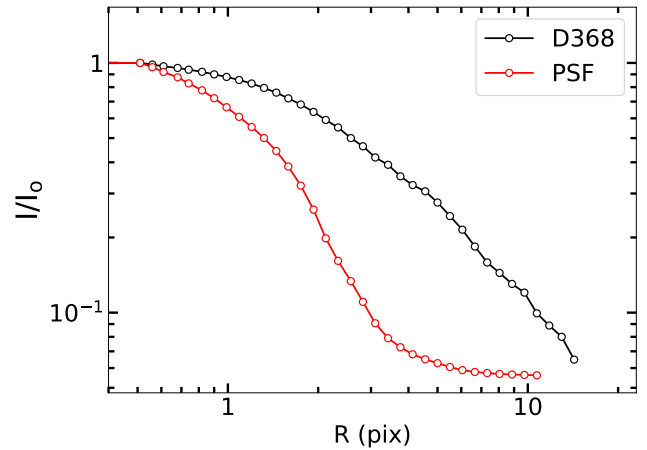


**Figure 4.** PSF profile (red) compared to that for one of the most compact clusters of the sample (D368: black), both normalised to their peak values in the V-band. These radial profiles are obtained using the IRAF task *ellipse*, at logarithmic steps increasing successively by 10%. The cluster profiles are clearly broader than the PSF profiles.

& Arnouts 1996). A star is considered to be suitable for PSF construction if it is isolated, and bright, but not saturated. We used various SExtractor output parameters to select these PSF stars. More than 1000 stars were used in each of the bands for this purpose (1234 in B, 1401 in V and 1328 in I). The resulting PSFs are shown in Fig. 3.

In order to illustrate that our selected SSCs are easily distinguishable from stars, we compare in Fig 4 the profile for one of the smallest SSCs with that of the PSF. Each displayed profile is an azimuthally averaged profile obtained as described in §2.1. In this illustration, both profiles are sampled in logarithmic steps successively increasing by 1%. Profiles generated for fitting purposes have linear steps of 1 pixel size for clusters and 0.5 pixel size for the PSF.

**Table 2.** Range and step of parameters values for the three fitted models

| Model<br>(1) | $r_d$ or $r_0$<br>(2) | $\gamma$ or $W_0$<br>(3) |
|--------------|-----------------------|--------------------------|
| Moffat-EFF   | 0.05–10;0.04          | 0.1–10;0.04              |
| King         | 0.05–10;0.10          | 2.0–15;0.10              |
| Wilson       | 0.05–10;0.10          | 2.0–15;0.10              |

Col (1): Model. Col (2): Moffat-EFF  $r_d$  or Dynamical (King or Wilson)  $r_0$  ranges and step size in pixels. Col (3): Moffat-EFF  $\gamma$  parameter or Wilson or King  $W_0$  parameter range and step size.

### 3.3 $\chi^2$ method and errors on derived parameters

In order to extract structural parameters from SBPs, we used the  $\chi^2$ -minimisation technique. We define  $\chi^2$  as:

$$\chi^2 = \sum_{i=1}^{N_{\text{pts}}} \frac{(I_{\text{obs}_i} - \tilde{I}_{\text{model}_i})^2}{\sigma_i^2}, \quad (9)$$

where  $I_{\text{obs}_i}$  and  $\tilde{I}_{\text{model}_i}$  are the  $i^{\text{th}}$  point in the observed SBP and PSF-convolved model profile, respectively. The summation is over  $N_{\text{pts}}$ , within the fitting radius,  $R_{\text{fit}}$ . The  $\sigma_i$  term is the  $I_{\text{err}}$  of the azimuthally averaged  $i^{\text{th}}$  isophote, as calculated by the *ellipse* task.

The convolution of the model with the PSF was performed with the Fortran routine CONVLV from NUMERICAL RECIPES (Press et al. 1992) which performs a FFT. For this purpose, we sampled both the PSF and the model at linear steps of 0.5 pixels which is two times the sampling of the objects.

The  $\chi^2$  fitting technique is implemented using a Fortran program developed for this purpose. The best-fitting parameters were obtained using a two-step procedure: in the first step, we used a coarse grid in the parameter space to obtain a preliminary minimum  $\chi^2$ . In the second step, we used ten-times better steps and searched for minimum  $\chi^2 \equiv \chi_{\text{min}}^2$  around the preliminary parameters set, to cover a range of four-times the coarse step. In Tab. 2, we give the range and the coarse step size for the parameters. The fitting procedure starts with coarse grids. Once a local minimum is found, the fine grid is used. We repeated the second step around the next two local minima of the first step. In all cases, the best-fit parameter set using fine steps is around the values corresponding to the minimum  $\chi^2$ . This two-step procedure ensures that the recovered parameters have a numerical precision better than the coarse step. This also resulted in a parameter set of nearly one thousand models that satisfy the condition  $\chi^2 - \chi_{\text{min}}^2 < 1$ .

The errors on the best-fit parameters for all 99 SSCs were obtained based on the  $\chi^2$  statistics. We considered parameter values of all our models for which  $\chi^2 - \chi_{\text{min}}^2 < 1$ , as a set of acceptable values within 1- $\sigma$  confidence limit. We show this set of parameters in  $\gamma$  vs  $r_d$  plane as error ellipses for 10 of our objects for the Moffat-EFF profile fits in Fig. 5. The error on  $r_d$  and  $\gamma$  correspond to the projections of the ellipse along the x-axis and y-axis, respectively. We would like to note that the best-fit parameters are not necessarily at the centre of the ellipse, implying the errors on the positive and negative sides are not always the same. A clear

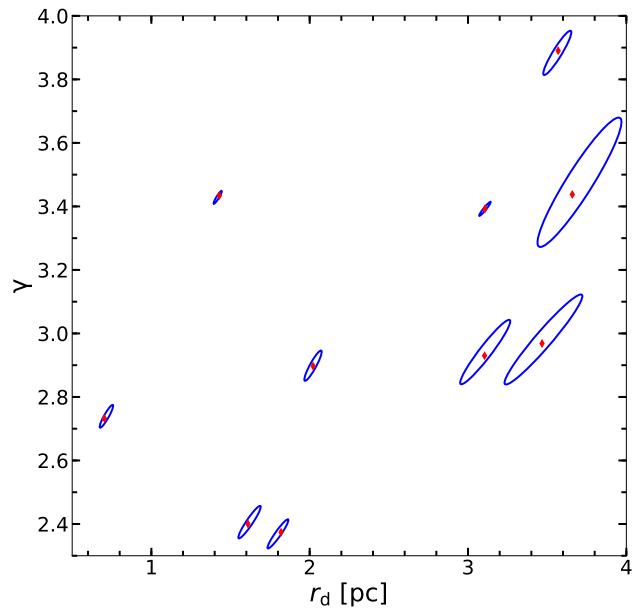


**Figure 5.** Error ellipses (1- $\sigma$  confidence intervals) of the parameters  $r_d$  and  $\gamma$  of models satisfying the criterion  $\chi^2 - \chi_{\text{min}}^2 < 1$  for the brightest 10 observed clusters of the sample. The errors on both axes correspond to the projections of the ellipse along x-axis and y-axis. The best-fitted parameters are shown with red diamonds.

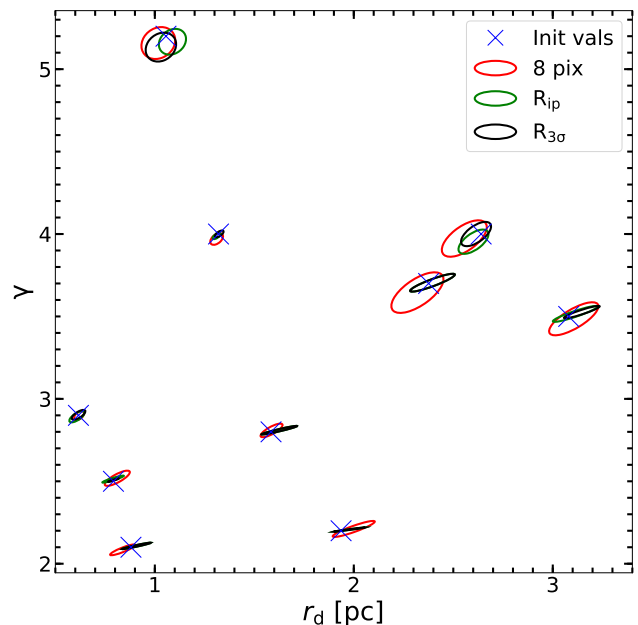


**Figure 6.** Error ellipses (1- $\sigma$  confidence intervals) of the parameters  $r_d$  and  $\gamma$  of models satisfying the criterion  $\chi^2 - \chi_{\text{min}}^2 < 1$  for 10 synthetic clusters that mimic the properties of the clusters of the sample. For each synthetic cluster, parameter values for 3  $R_{\text{fit}}$  values are shown:  $R_{\text{fit}}=8$  pixels (red),  $R_{\text{ip}}$  (green) and  $R_{3\sigma}$  (black). The initial values are shown by crosses, which are inside the error ellipses even with the  $R_{\text{fit}}=8$  pixels.

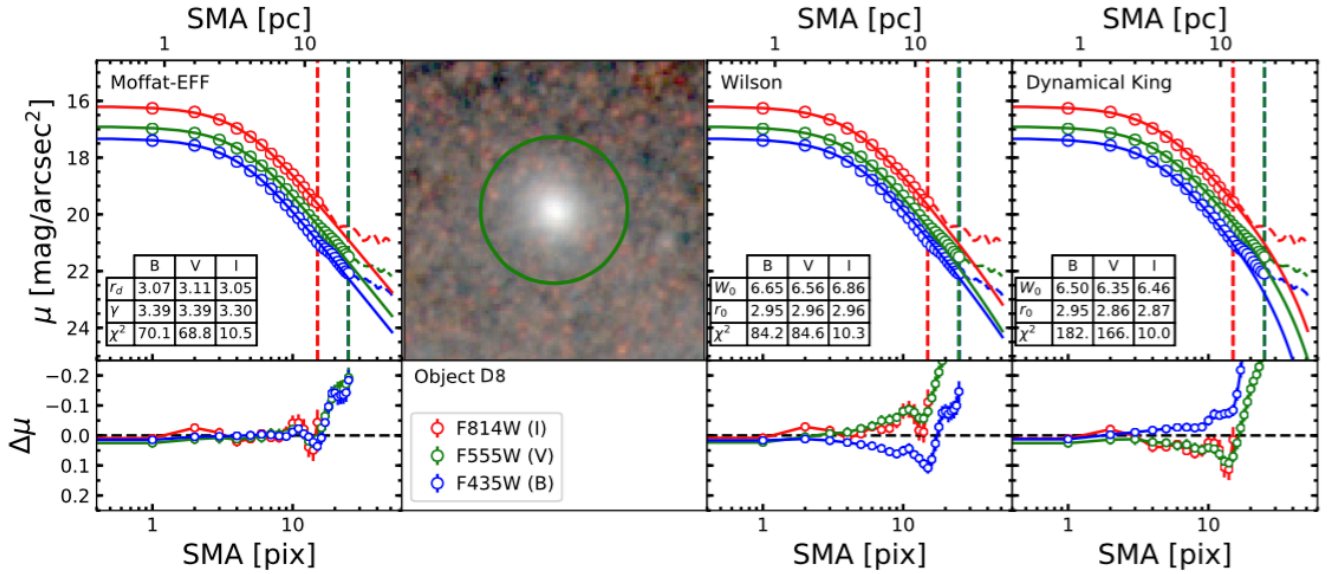


**Figure 7.** Illustration of the dynamical model fitting of the observed profiles with Moffat-EFF (left-most), Wilson (third from left) and Dynamical King (right-most). Profiles for SSC D8 in the filters B (blue), V (green) and I (red) are shown, and the fitting radius is indicated with dashed vertical lines following the same colour code. In this particular case, the  $R_{\text{fit}}$  corresponding to filters B and V coincide. In the bottom panels, the corresponding residuals ( $\Delta\mu = \mu_{\text{obs}} - \mu_{\text{model}}$ ) are shown. An RGB cut-out image of the cluster formed using I(R), V(G) and B(B) band images is shown, with a circle indicating the  $R_{\text{fit}}$  of the V-band. Each fitted point is shown by circles for radius  $\leq R_{\text{fit}}$ , and by dashed lines beyond that. The error bars are shown both in the fittings and the residuals, but are smaller than the symbol size for the great majority of points. The best-fit parameter values and the  $\chi^2_{\text{min}}$  for each fit are shown in the embedded tables. The electronic version contains plots such as this for all the 99 SSCs.

tendency is seen for errors being larger for larger values of the parameters. These  $1\text{-}\sigma$  confidence limits are reported as the errors on  $r_d$  and  $\gamma$  for all the clusters in Tab. 3. A similar analysis was carried out to obtain the errors on the parameters of King and Wilson models, which are also reported in the table.

### 3.4 Fits on simulated clusters and minimum $R_{\text{fit}}$

As mentioned in §2.1, the choice of  $R_{\text{fit}}$  is crucial in determining reliable structural parameters. With the aim of determining the minimum number of pixels required for this, we carried out a profile fitting procedure on simulated clusters. The mock sample of clusters constituted 10 clusters, all following Moffat-EFF profiles and covering the extreme ranges of the parameter space. An rms noise is added to the simulated images, which are also convolved with the PSFs described in §3.2 in order to simulate the observational effects. The structural parameters of the mock sample were recovered following the same procedure as that for the sample clusters. For each cluster, we obtained structural parameters for several values of  $R_{\text{fit}}$ , starting at 6 pixels, and all the way up to  $R_{\text{fit}}=R_{3\sigma}$ .

For each of these  $R_{\text{fit}}$  values, we obtained the best-fit parameters as well as their error ellipses. We found that for  $R_{\text{fit}} < 8$  pixels,  $\chi^2_{\text{min}}$  values in general were greater than  $3 \times \nu$  and hence do not satisfy our selection criteria. In Fig. 6, we show the results of the simulations in  $\gamma$  vs  $r_d$  plane for three values of  $R_{\text{fit}}$ : 1.  $R_{\text{fit}}=R_{3\sigma}$ , 2.  $R_{\text{fit}}=R_{\text{ip}}$ , and 3.  $R_{\text{fit}}=8$  pixels. As expected,  $R_{\text{fit}}=R_{3\sigma}$  has the least error, with the maximum error being for the  $R_{\text{fit}}=8$  pixels. Even in the

latter case, the recovered values are in good agreement with respect to the initial values. Thus, we conclude from these simulations that the parameters values recovered with  $R_{\text{fit}}=8$  pixels for our observed sample are reliable.

### 3.5 Method to select the best model

A fit is considered to be good if  $\chi^2_{\text{min}}$  is of the order of the degrees of freedom ( $\nu$ ) (Wall & Jenkins 2003), which in our general case is  $\nu = N_{\text{pts}} - 2$ . However, in fitting SBPs it is common to obtain  $\chi^2_{\text{min}} < \nu$ , even when fits are good (McLaughlin & van der Marel 2005). This is because, it is necessary to sample the central parts at steps of at least 1 pixel in order to define the SBPs, which is more than a factor of two oversampled with respect to the typical PSF values. This makes the SBP values at successive points not completely independent of each other, i.e.  $\sigma_i$  of successive points are correlated making  $\chi^2_{\text{min}} < \nu$ . We used the rms errors in the azimuthally averaged intensities as  $\sigma_i$  in the  $\chi^2$  equation, and hence there may be some contribution to the  $\sigma_i$  from real azimuthal variations, which also will make  $\chi^2_{\text{min}} < \nu$ . Some SSCs have  $\chi^2_{\text{min}} > 3\nu$ , which implies the best-fit model does not represent perfectly the observed SBP.

In Fig. 7, we show the results for the best fitting parameters for an illustrative cluster, for each of the three model profiles. In the left-most panel, we show the results for the best-fitting Moffat-EFF model, and in the other two panels, we show the results for the best-fitting Wilson and King models. In the second panel, we show an RGB image for the same cluster. In each panel, fits are shown for the three bands used in this analysis, along with the best-fit model



**Table 3.** Best-fit parameters in filter V for Moffat-EFF, King and Wilson models.

| ID  | Npts | Model | $\chi^2_{\min}$ | $W_0$ or $\gamma$       | $r_0$ or $r_d$<br>(pc) | $\mu_0$<br>(mag/arcsec <sup>2</sup> ) | $\log I_0$<br>( $L_{\odot}/\text{pc}^2$ ) |
|-----|------|-------|-----------------|-------------------------|------------------------|---------------------------------------|---|
| (1) | (2)  | (3)   | (4)             | (5)                     | (6)                    | (7)                                   | (8)                                       |
| D1  | 19   | M     | 12.69           | $2.73^{+0.04}_{-0.03}$  | $0.70^{+0.06}_{-0.03}$ | $13.55^{+0.11}_{-0.06}$               | $5.16^{+0.07}_{-0.04}$                    |
|     |      | K     | 22.92           | $8.70^{+0.04}_{-0.05}$  | $0.92^{+0.10}_{-0.19}$ | $13.55^{+0.15}_{-0.28}$               | $5.16^{+0.11}_{-0.20}$                    |
|     |      | W     | 10.04           | $8.76^{+0.08}_{-0.01}$  | $0.84^{+0.19}_{-0.10}$ | $13.55^{+0.29}_{-0.14}$               | $5.16^{+0.21}_{-0.30}$                    |
| D4  | 9    | M     | 11.57           | $2.97^{+0.15}_{-0.13}$  | $3.47^{+0.29}_{-0.27}$ | $16.50^{+0.46}_{-0.42}$               | $3.98^{+0.33}_{-0.30}$                    |
|     |      | K     | 11.65           | $7.86^{+7.14}_{-1.36}$  | $3.56^{+0.40}_{-0.10}$ | $16.50^{+10.1}_{-1.93}$               | $3.98^{+7.15}_{-1.36}$                    |
|     |      | W     | 11.72           | $8.95^{+6.05}_{-1.55}$  | $3.56^{+0.40}_{-0.10}$ | $16.50^{+8.57}_{-2.20}$               | $3.98^{+6.06}_{-1.55}$                    |
| D7  | 11   | M     | 1.46            | $2.37^{+0.04}_{-0.05}$  | $1.82^{+0.05}_{-0.10}$ | $16.85^{+0.09}_{-0.15}$               | $3.84^{+0.07}_{-0.11}$                    |
|     |      | K     | 18.86           | $14.96^{+0.04}_{-2.56}$ | $2.52^{+0.19}_{-0.10}$ | $16.85^{+0.28}_{-3.62}$               | $3.84^{+0.20}_{-2.56}$                    |
|     |      | W     | 19.42           | $14.96^{+0.04}_{-1.46}$ | $2.52^{+0.19}_{-0.10}$ | $16.85^{+0.28}_{-2.06}$               | $3.84^{+0.20}_{-1.46}$                    |
| D8  | 25   | M     | 68.86           | $3.39^{+0.02}_{-0.02}$  | $3.11^{+0.04}_{-0.04}$ | $16.90^{+0.07}_{-0.07}$               | $3.82^{+0.05}_{-0.05}$                    |
|     |      | K     | 166.94          | $6.35^{+0.09}_{-0.09}$  | $2.86^{+0.20}_{-0.10}$ | $16.90^{+0.31}_{-0.19}$               | $3.82^{+0.22}_{-0.13}$                    |
|     |      | W     | 84.65           | $6.56^{+0.19}_{-0.10}$  | $2.96^{+0.19}_{-0.01}$ | $16.90^{+0.38}_{-0.14}$               | $3.82^{+0.27}_{-0.10}$                    |
| D10 | 9    | M     | 3.84            | $2.40^{+0.06}_{-0.04}$  | $1.61^{+0.09}_{-0.07}$ | $16.39^{+0.15}_{-0.12}$               | $4.02^{+0.11}_{-0.08}$                    |
|     |      | K     | 13.08           | $14.96^{+0.04}_{-3.15}$ | $2.25^{+0.19}_{-0.10}$ | $16.39^{+0.28}_{-4.46}$               | $4.02^{+0.20}_{-3.16}$                    |
|     |      | W     | 13.62           | $14.96^{+0.04}_{-1.85}$ | $2.25^{+0.19}_{-0.10}$ | $16.39^{+0.28}_{-2.63}$               | $4.02^{+0.20}_{-1.86}$                    |
| D14 | 14   | M     | 19.00           | $3.89^{+0.06}_{-0.07}$  | $3.57^{+0.09}_{-0.11}$ | $17.35^{+0.16}_{-0.18}$               | $3.64^{+0.11}_{-0.13}$                    |
|     |      | K     | 29.65           | $5.20^{+0.10}_{-0.10}$  | $3.21^{+0.10}_{-0.10}$ | $17.35^{+0.20}_{-0.20}$               | $3.64^{+0.14}_{-0.14}$                    |
|     |      | W     | 22.75           | $5.20^{+0.04}_{-0.14}$  | $3.39^{+0.10}_{-0.19}$ | $17.35^{+0.15}_{-0.33}$               | $3.64^{+0.11}_{-0.24}$                    |

Col (1): Cluster name. Col (2): Number of points used in the fitting procedure. Col (3): Fitted model, M (Moffat-EFF), (K) Dynamical King, (W) Wilson. Col (4): Minimum value of  $\chi^2$  obtained for the selected model in Col (3). Col (5): Shape parameter,  $W_0$  for Wilson and Dynamical King models, and  $\gamma$  for Moffat-EFF. Col (6): Scale parameter,  $r_0$  for Wilson and King, and  $r_d$  for Moffat-EFF. Col (7–8): Central surface brightness in magnitude and luminosity units, respectively. The full table is shown in the electronic edition; a portion is shown here for guidance.

parameters in each band. The  $R_{\text{fit}}$  in each band is indicated by vertical lines and  $R_{\text{fit}}$  for the V band is shown in the RGB image.  $R_{\text{fit}}$  values in B and V bands match in general, whereas in the I band, it is generally smaller. Bottom panels show the residual  $\Delta\mu = \mu_{\text{obs}} - \mu_{\text{model}}$ .

In most cases,  $\chi^2_{\min}$  values for the best-fit Moffat-EFF, King and Wilson models are not very different, implying that the fits are equally good for more than one model. [McLaughlin & van der Marel \(2005\)](#) proposed a method to determine quantitatively the best among these models. We adopted their technique for fits obtained for each filter for every cluster. This method consists of defining a  $\Delta\chi^2$  as:

$$\Delta\chi^2 = \frac{\chi^2_{\text{alt}} - \chi^2_{\text{ref}}}{\chi^2_{\text{alt}} + \chi^2_{\text{ref}}}, \quad (10)$$

where  $\chi^2_{\text{ref}}$  and  $\chi^2_{\text{alt}}$  are the  $\chi^2_{\min}$  values of the reference model and the model to be compared. Two models are considered to be equally good if  $|\Delta\chi^2| \leq 0.2$ , whereas the reference model is good for  $\Delta\chi^2 > 0.2$ .

In Fig. 8, we show the  $\Delta\chi^2$  distributions for all the 99 SSCs with Moffat-EFF as the reference model. Around 45% of the clusters have  $|\Delta\chi^2| \leq 0.2$ , indicating that all the three models are fit equally well for these clusters. Moffat-EFF models are good fits for 95–97% of the SSCs, with only 3–5% of SSCs requiring King or Wilson models. These conclusions also apply to the fits in the other two bands, but with the best-fit Moffat-EFF percentage being around 15% lower.

Thus, in general, M82 SSCs are well represented by Moffat-EFF models, and hence we will use the parameters obtained by Moffat-EFF in the V-band as the characteristic values for all clusters. An examination of the half-light

radius  $R_h$  values indicates that even for the 45% of the clusters represented equally well by any one of the three models, Moffat-EFF parameters are more reliable than the other two models. In Fig 9, we illustrate this, where we plot the  $R_h$  of King models against those obtained from Moffat-EFF models for the 99 SSCs. The error bars on  $R_h$  are obtained by propagating the errors on the basic derived parameters for each model (See §3.3). Clusters for which fits are equally good with King and Moffat-EFF models are distinguished from those for which Moffat-EFF models are good. It can be seen that  $R_h$  values for King models are overestimated in several cases independent of if King is a good fit or not.

In Table 3, we show the best-fitted shape ( $W_0$  or  $\gamma$ ), scale ( $r_0$  or  $r_d$ ) and central surface brightness ( $\mu_0$  and  $I_0$ ) parameters for all the three models along with the  $\chi^2_{\min}$  values for the fits in the V-band. Data for each cluster are organised in three rows: the first row shows the results for Moffat-EFF, the second row for King models and the third row for Wilson models. For the last four columns, we give their respective error bars. The error bars on shape and scale parameters are based on the analysis in §3.3. The error bars in the central surface brightness are based on these errors propagated in quadrature, following the prescription of [McLaughlin & van der Marel \(2005\)](#). The  $\chi^2_{\min}$  given in Column 4 is related to the reduced  $\chi^2_{\nu}$  by the number of degrees of freedom  $\nu$ , which in our case is equal to  $N_{\text{pts}} - 2$  given that we have two fitted parameters. Hence,  $\chi^2_{\nu} = \frac{\chi^2_{\min}}{N_{\text{pts}} - 2}$ . For all of our clusters,  $\chi^2_{\nu} < 3$  in the V-band for at least one of the three models.

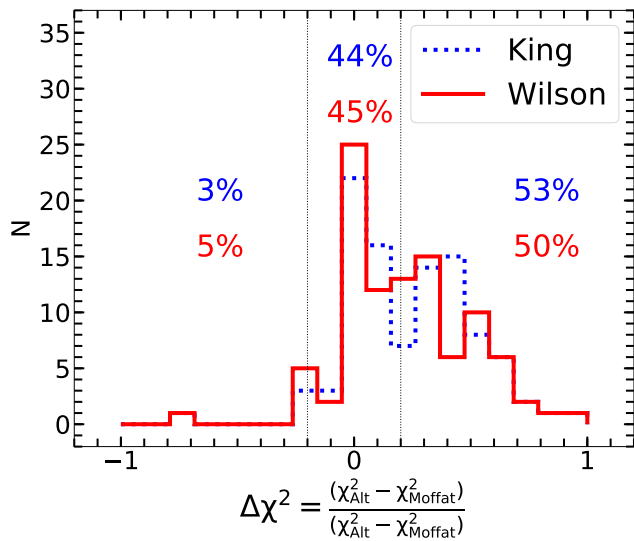


**Figure 8.**  $\Delta\chi^2$  distributions of the Moffat-EFF selected as reference model, compared with King (blue dotted) and Wilson (red solid) models for fits in the V-band. The reference and the comparison models are considered to be equally good for  $|\Delta\chi^2| \leq 0.2$ , which is signalled by the vertical dotted lines. The three columns of numbers appearing in percentage correspond to the King vs Moffat-EFF (blue) and Wilson vs Moffat-EFF (red), for  $\Delta\chi^2 < -0.2$ ,  $|\Delta\chi^2| \leq 0.2$ , and  $\Delta\chi^2 > 0.2$ , respectively. For 44–45% of the clusters, the fits are equally good for any of the three models, with Moffat-EFF model providing a better fit ( $\Delta\chi^2 > 0.2$ ) for a further 50–53%. For only 3–5% of the clusters ( $\Delta\chi^2 < -0.2$ ), King or Wilson models provide a better fit than Moffat-EFF model.

### 3.6 Comparison with GALFIT and ISHAPE

GALFIT (Peng et al. 2010) and ISHAPE (Larsen 1999) are two widely used tools for obtaining structural parameters of extragalactic clusters. In order to ensure that there are no systematic offsets in the values of structural parameters obtained by our fitting tool with those obtained with these two tools, we carried out the fits with the Moffat-EFF profiles on all our sample clusters with these two tools. The PSF images, as well as the fitting radius for each cluster are retained from our analysis. In the case of ISHAPE, we oversampled our PSF image by a factor of ten using the tool *magnify* in IRAF, as required by the code. Fittings were carried out on 2-D images of  $101 \times 101$  pixel cut-outs. Both these codes have their own algorithm for background determination. The  $\gamma$  values are left free for GALFIT, whereas for ISHAPE, we used our best-fit  $\gamma$  values for each cluster. In Fig. 10, we compare our  $r_d$  values with those from GALFIT and ISHAPE. We observe that in general, our values are in excellent agreement with those of GALFIT, and are consistent within the errors with those of ISHAPE, but with a slope of 1.3, instead of unity. The lengths of the error bars in GALFIT are very similar to ours, whereas ISHAPE values have larger error bars. We checked that these error bars and the values do not vary much for a fixed value of  $\gamma = 3$ .

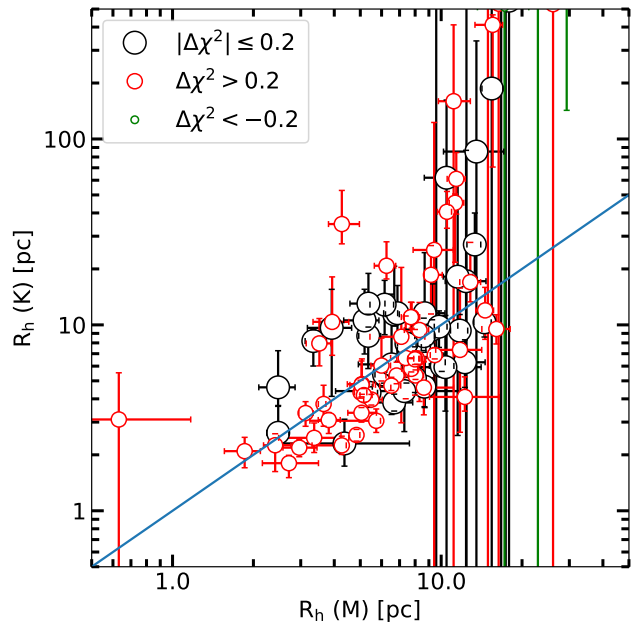


**Figure 9.** Half-light radius  $R_h$  of King models against those obtained from Moffat-EFF models for the 99 SSCs. Clusters are colour and size coded to indicate equally good fits with King and Moffat-EFF models (black large circles), better fit with Moffat-EFF models (red medium-sized circles), and those well represented with King models (green small circles). The  $R_h$  derived from both the models agree with each other for  $R_h \lesssim 10$  pc, independent of which model produced the best fit. Beyond this radius, the error bar on the  $R_h$  derived from King models is systematically larger than those for the Moffat-EFF models. We note that this is even true for the three clusters for which King model produced the best fit (green vertical lines).

## 4 RESULTS AND DISCUSSIONS

In the previous section, we concluded that Moffat-EFF models adequately represent all our subsample of 99 SSCs. Model-fitting directly gives us four parameters, namely  $r_d$ ,  $\gamma$ ,  $\mu_0$  and  $L_{tot}$ . Core radius  $R_c$ , the radius at which the surface brightness is half its peak value, is related to  $r_d$  through Eqn. 7. The half-light radius  $R_h$ , is another parameter that can be calculated from these parameters (see §3.5). Dynamical analysis of the fitted model profiles, along with a knowledge of mass-to-light ratio for M82 SSCs, allows us to calculate four more parameters: mass, the central velocity dispersion  $\sigma_0$ , central mass density  $\rho_0$  and central mass surface density  $\Sigma_0$ . Not all these parameters are independent of each other. Evolved objects like GCs show a tight inverse correlation between  $R_c$  and  $\mu_0$  (Kormendy 1985). These correlations are part of the Fundamental Plane for GCs (Djorgovski 1995; McLaughlin 2000). A detailed analysis of all the derived parameters will be carried out in a forthcoming paper. In this paper, we will characterise the basic parameters obtained in the three bands.

### 4.1 Colour-dependence of the derived parameters

We have carried out independent analysis of SBPs in three filters for all our sample SSCs to study the possible colour-

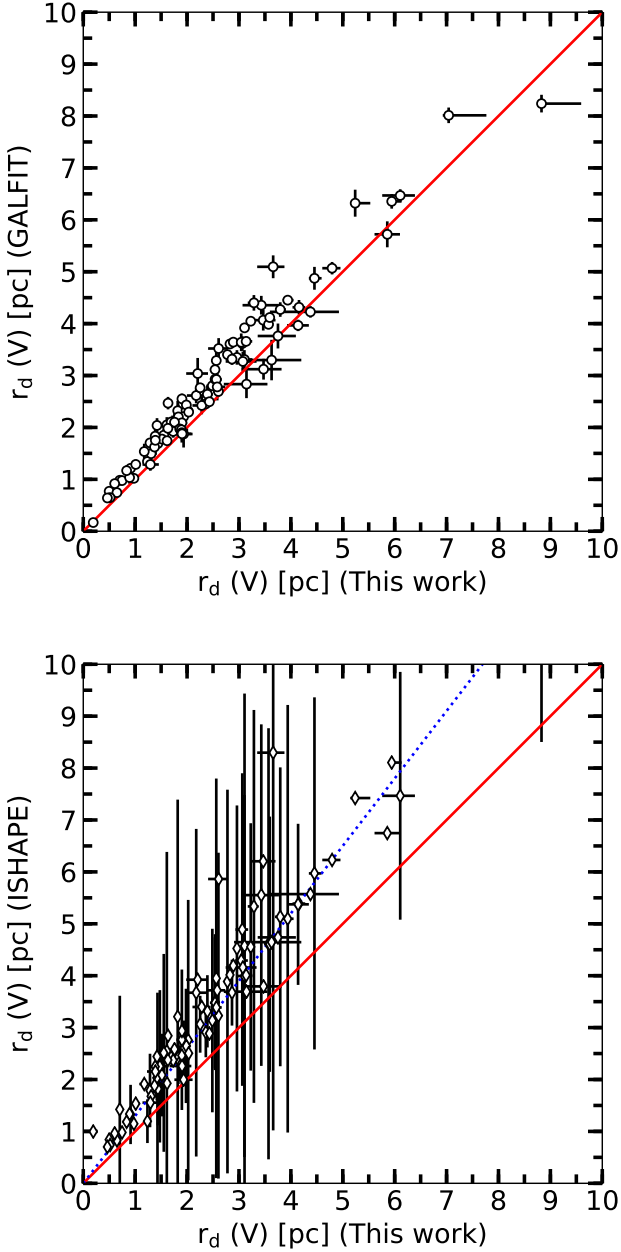


**Figure 10.** Comparison between Moffat-EFF  $r_d$  obtained with our own code with that obtained using GALFIT (top) and ISHAPE (bottom). The identity function is shown with a red solid line. Values from our code are in excellent agreement with that from GALFIT, whereas the ISHAPE-derived values are systematically higher by  $\sim 30\%$ , which is indicated by a blue-dotted line of slope=1.3.

dependence of the derived parameters. In Figs. 11, 12, and 13, we compare the distribution of  $r_d$ ,  $\gamma$ , and  $\mu_0$  for Moffat-EFF models in the three filters. The intention of showing these distributions is to compare the shape, as well as the center of the distributions. Median values are indicated in all the plots by vertical dashed lines.

Median values of  $r_d$  in the three filters are very similar with a value  $\sim 2.0$  pc. In all the three filters, the distribution is asymmetric with its peak lying at  $\sim 1$  pc to the left of

the median value, and having a long tail that reaches up to  $\sim 7-9$  pc. The behaviour of  $\gamma$  distribution is very similar to that of  $r_d$  with the median value of  $\gamma \sim 3.0$  for the three filters.  $\mu_0$  median values in the three filters are:  $\mu_0(\text{B})=19.2$ ,  $\mu_0(\text{V})=18.5$ ,  $\mu_0(\text{I})=17.5$  mag arcsec $^{-2}$ . From these plots, we conclude that the distributions in the three filters are similar. Hence, we use the values in the V band in the rest of our analysis.

#### 4.2 Functional form of $\gamma$ distribution

Following the seminal study of Elson et al. (1987), power-law form of the SBPs represented by the Moffat-EFF profile, is considered to be the characteristic feature of young SSCs. On the other hand, King profiles (King 1962) are applicable to more evolved systems such as GCs. Elson et al. (1987) found the power-law form extends to beyond the tidal radius in young clusters. They argue that clusters take around 2 to 3 orbital periods to get rid of the stars outside the tidal radius, and hence, have to be older than  $\sim 1$  Gyr to show a King SBP. Until that time, the escaped stars would be located in an unbound halo.

Mackey & Gilmore (2003a) analysed the SBPs obtained from HST images of a sample of 53 LMC clusters using Moffat-EFF profiles. With as much as 25 clusters in this sample being younger than  $\sim 1$  Gyr, this happens to be the only case where young and intermediate-age well-resolved clusters have been analysed using a uniform set of Moffat-EFF parameters. For this reason, the parameter set obtained by Mackey & Gilmore (2003a) has become the benchmark against which parameters of SSCs in other galaxies have been compared with. Our analysis of nearly 100 intermediate-age (50–300 Myr) SSCs, offers an opportunity to understand the transition from power-law shaped young clusters to King profile shaped GCs.

The  $\gamma$  measures the slope of the power-law SBP at large radii (see Eqn. 6). A  $\gamma=2$  corresponds to the case of a King profile with an infinite value of concentration parameter, and infinite mass. For real clusters,  $\gamma > 2$ . The higher the value of  $\gamma$ , the steeper is the outer slope. In Fig 14 (top panel), we show the distribution of  $\gamma$  for M82 SSCs. The distribution is well represented by a log-normal function of  $\sigma \log(\gamma) = 0.08$ , centered at  $\gamma=2.88$ , which is close to the median value of 3.0. This value agrees well with the median value found for clusters in the LMC and other nearby galaxies (Portegies Zwart et al. 2010). In the bottom panel, we compare the distribution of  $\gamma$  for the disk clusters in M82, with those in other galaxies (LMC/SMC, M83, NGC1313 and NGC628) where measurements of  $\gamma$  had been carried out. Parameters for M83 come from the study of Ryon et al. (2015) and NGC1313 and NGC628 from Ryon et al. (2017). These parameters were obtained using GALFIT. LMC/SMC cluster parameters come from the study of Mackey & Gilmore (2003a,b). We divided the sample in these galaxies into young ( $< 50$  Myr), intermediate-age (50–500 Myr) and old ( $> 500$  Myr) clusters. For the sake of comparison with M82 disk SSCs, we use the sample of intermediate-age clusters. The subsample of intermediate-age clusters includes 335 in M83, 235 in NGC628, 147 in NGC1313, and 24 in LMC/SMC.

Our distribution compares well with that in the LMC/SMC, both being log-normal centered around  $\gamma=2.9$ . On the other hand,  $\gamma$ -values distribute over a wide range

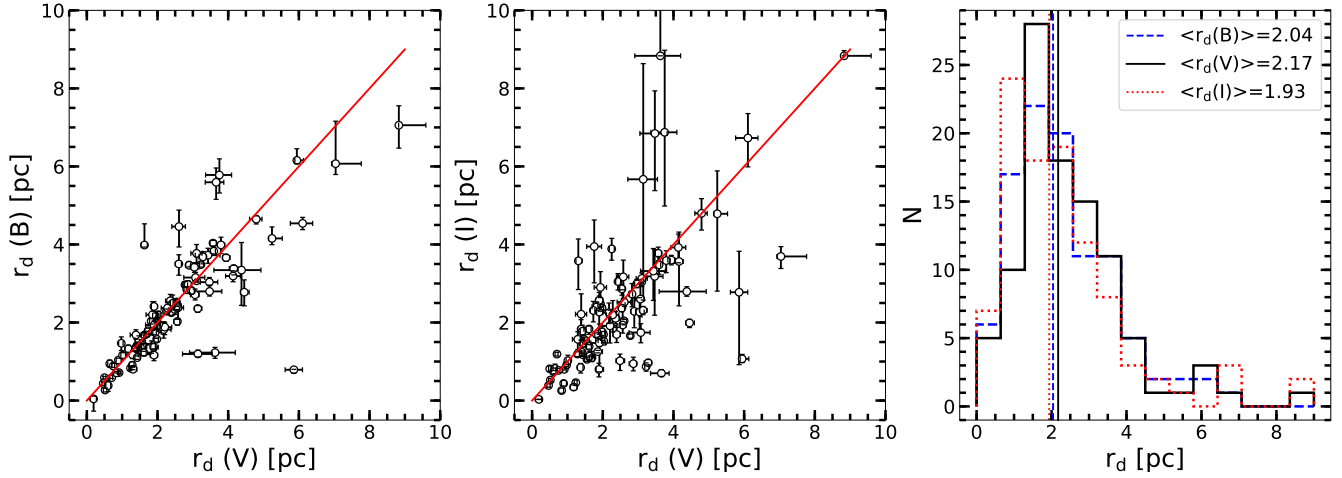


**Figure 11.** Comparison of  $r_d$  values obtained in three filters:  $r_d$  (B) vs  $r_d$ (V) (left), and  $r_d$  (I) vs  $r_d$ (V) (middle). The red solid line shows the identity function. Histogram of the Moffat-EFF  $r_d$  of the 99 selected clusters for the B (blue dashed line), V (black solid line) and I (red dotted line) are shown in the right panel. The median of each distribution is shown by a vertical line of the same colour code.

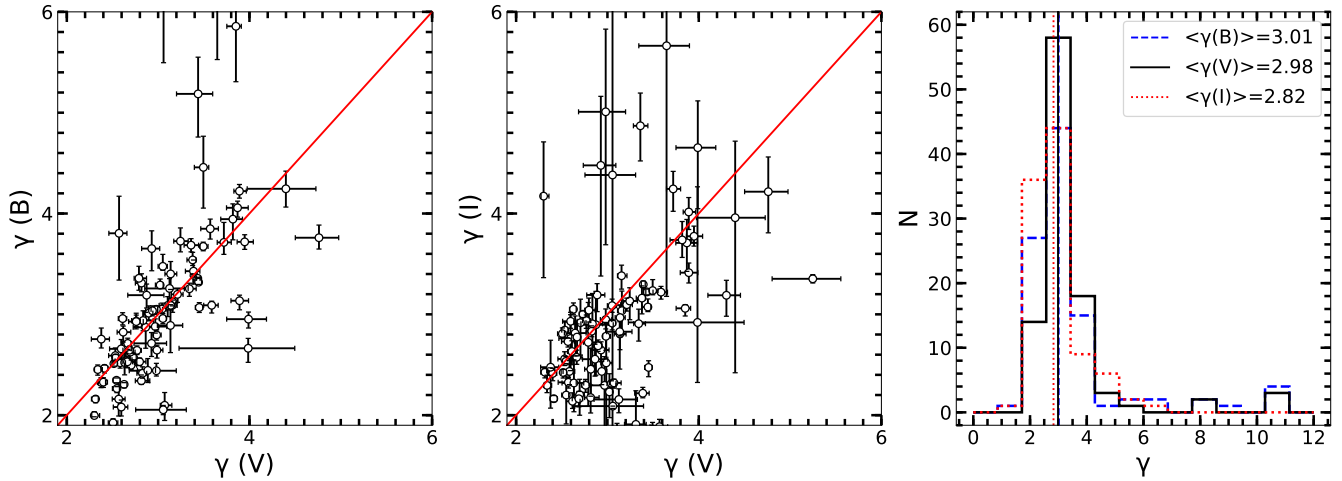


**Figure 12.** Comparison of  $\gamma$  values obtained in three filters:  $\gamma$  (B) vs  $\gamma$ (V) (left), and  $\gamma$  (I) vs  $\gamma$ (V) (middle). The red solid line shows the identity function. Histogram of the Moffat-EFF  $\gamma$  of the 99 selected clusters for the B (blue dashed line), V (black solid line) and I (red dotted line) are shown in the right panel. The median of each distribution is shown by a vertical line of the same colour code.

in other galaxies, peaking at the minimum value of  $\gamma=2$ , and decreasing almost linearly (power-law) on this plot for higher values. For M83, we show the distribution of old clusters also. The sample of intermediate-age clusters of M83 shows the same behaviour as for the old sample, and hence the power-law tendency seems to be independent of evolutionary stage.

Elson et al. (1987) argued that  $2.5 < \gamma < 3.2$  correspond to density profiles in dissipationless systems. Cluster formation in their parent molecular cloud should be 100% efficient for the real clusters to be dissipationless. On the other hand, real clusters are expected to contain some residual gas within the cluster volume, which would be expelled from the cluster in the first 10 Myr, when massive stars end their lives as supernovae. The loss of gravitational energy of

the expelled gas-mass makes the cluster expand, which eventually shapes the outer part of the density profile (Bastian & Goodwin 2006). As the residual gas fraction or equivalently efficiency of cluster formation is expected to vary from one cluster to the other, real clusters are expected to have a wide range of  $\gamma$  values, in this scenario of cluster formation. An alternative scenario is that the gas continues to flow into the cluster volume even after the first supernovae explosions (Fujii et al. 2012; Parker et al. 2014). This is recently found to be the case in dense progenitor clouds of massive clusters in the Milky Way (Walker et al. 2015). Under this scenario, clusters do not necessarily expand freely following the multiple-supernovae explosions (Silich & Tenorio-Tagle 2017). It is likely that such clusters conserve their initial profile shape.

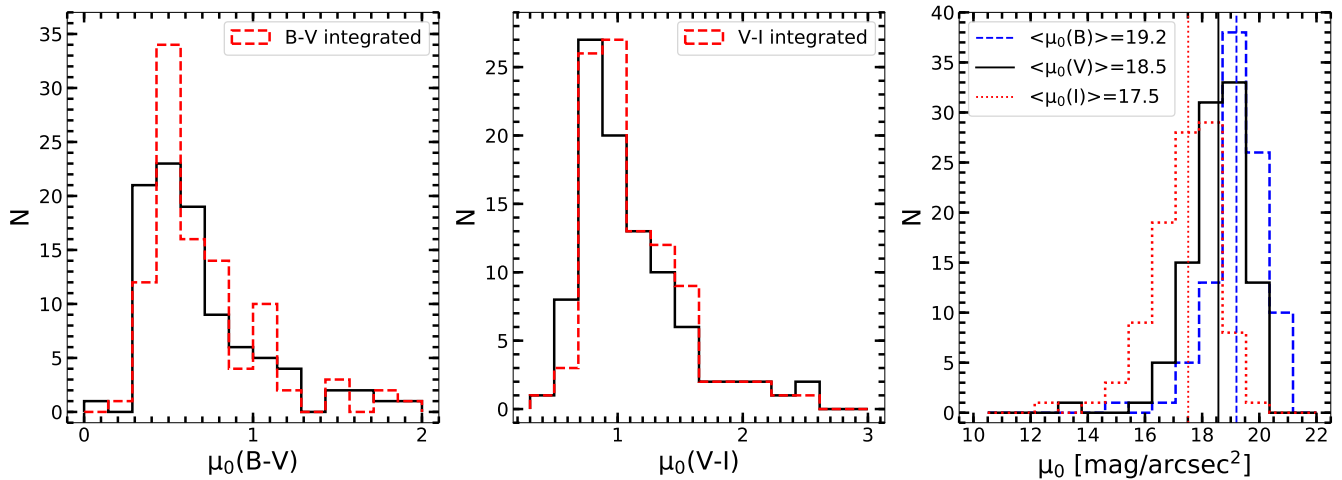


**Figure 13.** Central (black solid line) and integrated (red dashed line) colour histograms for  $\mu_0(B) - \mu_0(V)$  (left), and  $\mu_0(V) - \mu_0(I)$  (middle). Histogram of the Moffat-EFF  $\mu_0$  of the 99 selected clusters for the B (blue dashed line), V (black solid line) and I (red dotted line) are shown in the right panel. The median of each distribution is shown by a vertical line of the same colour code.

The log-normal form and the small spread in the  $\gamma$  value seem to support the latter scenario of cluster formation.

### 4.3 Functional form of $R_c$ distribution

We now discuss the distribution of  $R_c$  for our sample of SSCs. With  $R_c=0.1$  pc (Elson et al. 1992; Mackey & Gilmore 2003a) R136 in the LMC, often considered as the prototype for a young SSC, is one of the most compact SSCs known. Several young extragalactic SSCs also are found to have sub-parsec values of  $R_c$  (Portegies Zwart et al. 2010). Bastian et al. (2008) found a tendency for  $R_c$  to increase with age, which they interpreted as an evidence for expansion of SSCs.

In Fig. 15 (top panel), we show the distribution of the core radius  $R_c$  from our study. The distribution fits very well with a log-normal function centered at  $R_c = 1.73$  pc, and  $\sigma \log(\frac{R_c}{pc}) = 0.25$ . The median value of the distribution is 1.62 pc, which is close to the peak of the log-normal distribution. The study of Bastian et al. (2008) includes M82 disk SSCs from the spectroscopic sample of Konstantopoulos et al. (2009), for which they report a median value of  $R_c=2.2$  pc, which falls well within the range of our  $R_c$  values.

We used the same dataset as for  $\gamma$  to compare our  $R_c$  values with that in other galaxies. In the bottom panel, we show a plot comparing the distributions, where each distribution is fitted with a log-normal function. The central value ( $\overline{R_c}$ ) and  $\sigma$  of the function are given in Table 4. LMC and M83 clusters with ages similar to that in M82 disk (50–500 Myr) have mean  $R_c$  value higher and lower, respectively, as compared to that in M82. Incidentally, the morphological type of these galaxies change from SABc in M83 (de Vaucouleurs et al. 1991), Irr II/SBd in M82 (Mayya et al. 2005), to SBm in LMC (de Vaucouleurs et al. 1991). The progressive increase in mean  $R_c$  for similar-age clusters is probably suggesting that the morphological type has a role in core evolution at intermediate-ages. We also note that at older (>500 Myr) ages, M83 clusters have mean  $R_c$  similar

**Table 4.** Statistical properties of the Core Radius distributions in M82 and other nearby galaxies.

| (1)                  | $\overline{R_c}$ | $\sigma \log(\frac{R_c}{pc})$ | N   |
|----------------------|------------------|-------------------------------|-----|
| (1)                  | (2)              | (3)                           | (4) |
| M82 (Disk)           | 1.73             | 0.25                          | 99  |
| M83 (50–500 Myr)     | 1.42             | 0.51                          | 335 |
| M83 (>500 Myr)       | 1.66             | 0.56                          | 118 |
| LMC/SMC (50–500 Myr) | 2.29             | 0.39                          | 24  |

Col (1): Galaxy name and age range. Col (2): Peak value of  $R_c$ . Col (3): Standard deviation of the log-normal distribution. Col (4): Number of clusters in the specified age range.

to intermediate-age clusters of M82. This tendency of  $R_c$  increasing with age in M83 has been reported by Ryon et al. (2015). Similar tendency is also seen in LMC/SMC, which has been attributed to cluster expansion by Mackey et al. (2008).

### 4.4 $\gamma$ vs $R_c$ relation

Dynamical evolutionary models of clusters by Mackey et al. (2008) find a steady increase of both  $\gamma$  and  $R_c$  with age. Different physical processes are at work at different time scales. After the early steep increase in radius driven by residual gas expulsion, the mass-loss during stellar evolution is the principal process that drives the evolution of  $\gamma$  and  $R_c$  up to around 600 Myr. Such an evolution of  $\gamma$  and  $R_c$  are observed in the clusters in LMC and SMC (Mackey & Gilmore 2003a,b; Mackey et al. 2008).

In Figure 16, we plot  $R_c$  against  $\gamma$  for our sample of SSCs (top), as well as for SMC and LMC clusters from Mackey & Gilmore (2003a,b) and M83 from Ryon et al. (2015) (bottom). For the LMC/SMC clusters, a clear trend of the upper envelope of  $R_c$  increasing with increasing  $\gamma$ , as expected in the models of Mackey et al. (2008), is seen. For

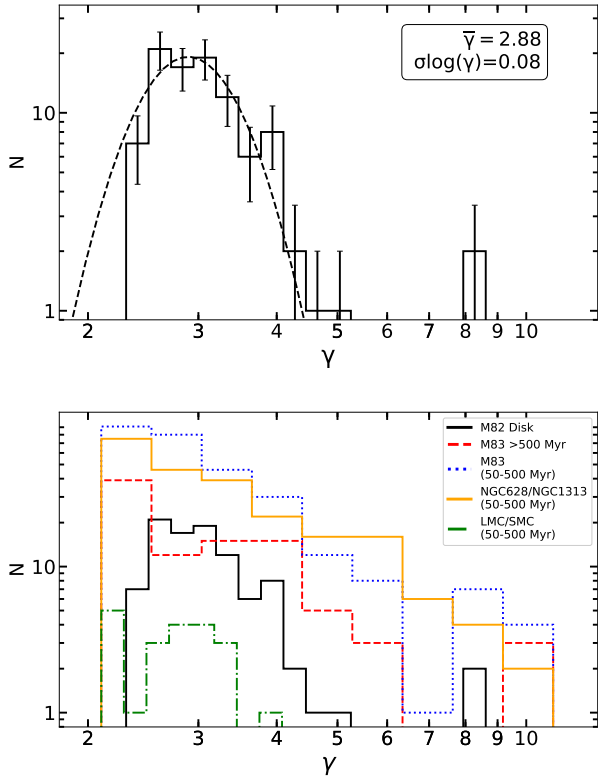


**Figure 14.** Upper panel: distribution of  $\gamma$  parameter for 99 M82 SSCs fitted with Moffat-EFF profile (histogram). The error bars are based on Poisson statistics. In dashed line, we show a log-normal fitting with a peak value of 2.88 and a standard deviation of  $\sigma\log(\gamma) = 0.08$ . Bottom panel: distribution of  $\gamma$  parameter in other nearby galaxies are compared with that of M82.

the M82 sample, the trend is weaker. But the trend is also weaker for LMC/SMC and M83 SSCs that have a similar range of ages as that of M82 SSCs. Hence, the observed values of  $R_c$  and  $\gamma$  in M82 are in broad agreement with the predictions of Mackey et al. (2008).

## 5 SUMMARY

In this work, we have carried out structural analysis of 99 intermediate-age (50–300 Myr) SSCs in the disk of M82 using the intensity profiles derived from HST images in F435W, F555W and F814W bands. These clusters have a narrow range of ages between 50–300 Myr, which provides an excellent opportunity to understand the structural parameters at ages intermediate between Young Super Star Clusters and Old Globular Clusters. Structural parameters were derived for the King, Wilson and Moffat-EFF models, using the standard  $\chi^2$  minimisation technique. Errors on the extracted parameters were determined based on the  $\chi^2$  statistics of the fitting models. Experiments on mock clusters were also carried out to authenticate the extracted parameters as well as their errors. In order to further validate our fitting technique, we obtained structural parameters with the Moffat-EFF profiles for our entire Sample of clusters using widely-used tools such as GALFIT and ISHAPE. We find excellent agreement with the values and their errors obtained

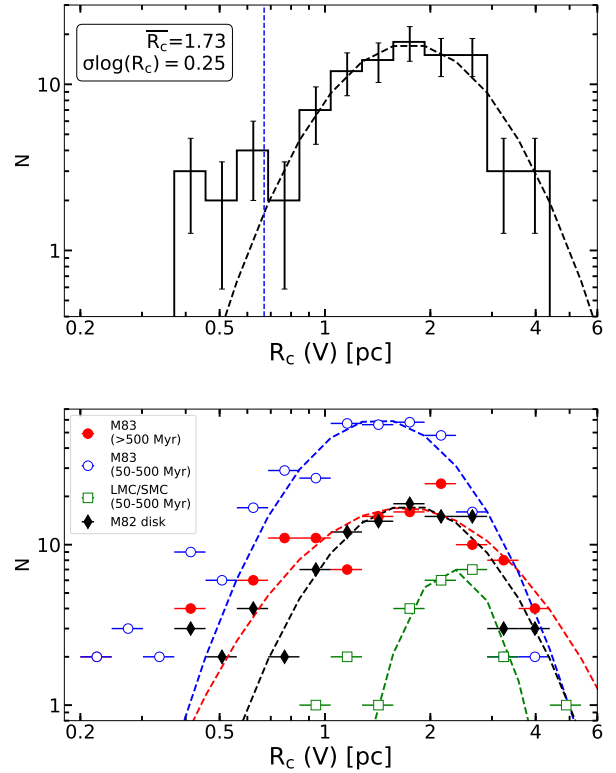


**Figure 15.** Upper panel: distribution of core radius  $R_c$  for 99 M82 SSCs fitted with Moffat-EFF profile (histogram). The error bars are based on Poisson statistics. In dashed line, we show a log-normal fit to the data, whose parameters are given in the top-left corner. The minimum reliable value according to the PSF is shown with a vertical blue dashed line. Bottom panel: comparison of binned distributions (symbols explained in the top-left corner) of  $R_c$  for M83 old (red), M83 intermediate-age (blue), LMC/SMC (green), M82 (black) SSCs. The horizontal bars correspond to the fixed logarithmic width used for binning. The best-fit log-normal function is shown by dashed lines following the same colour code as the binned data.

by GALFIT, whereas ISHAPE values have systematically large errors.

The observed profiles are in general well-fitted by all the three model profiles. Using quantitative criteria for discrimination between the models used, we find the majority of clusters ( $\sim 95\%$ ) is well-represented by Moffat-EFF profiles. We tabulate the fitted parameters in the F555W band for all the clusters using the three models, and analyse in detail the statistical properties of Moffat-EFF parameters. The distributions of  $\gamma$  and  $r_d$  in the three bands are similar, with very similar median values. The distribution of  $\gamma$  follows a log-normal shape around a central value of 2.88 and  $\sigma\log(\gamma) = 0.08$ . Values of  $\gamma < 3$  imply the existence of an extended halo in M82 clusters. The  $R_c$  distribution also follows a log-normal form with peak values of  $R_c = 1.73$  pc, and  $\sigma\log\left(\frac{R_c}{\text{pc}}\right) = 0.25$ . These values are large as compared to both Young SSCs and Old GCs, but compare well with the corresponding values for LMC intermediate-age clusters. Our  $\gamma$  and  $R_c$  distributions are also compared with the intermediate-age SSCs in M83, NGC1313 and NGC628. We find a larger spread of  $\gamma$  values in these galaxies as compared

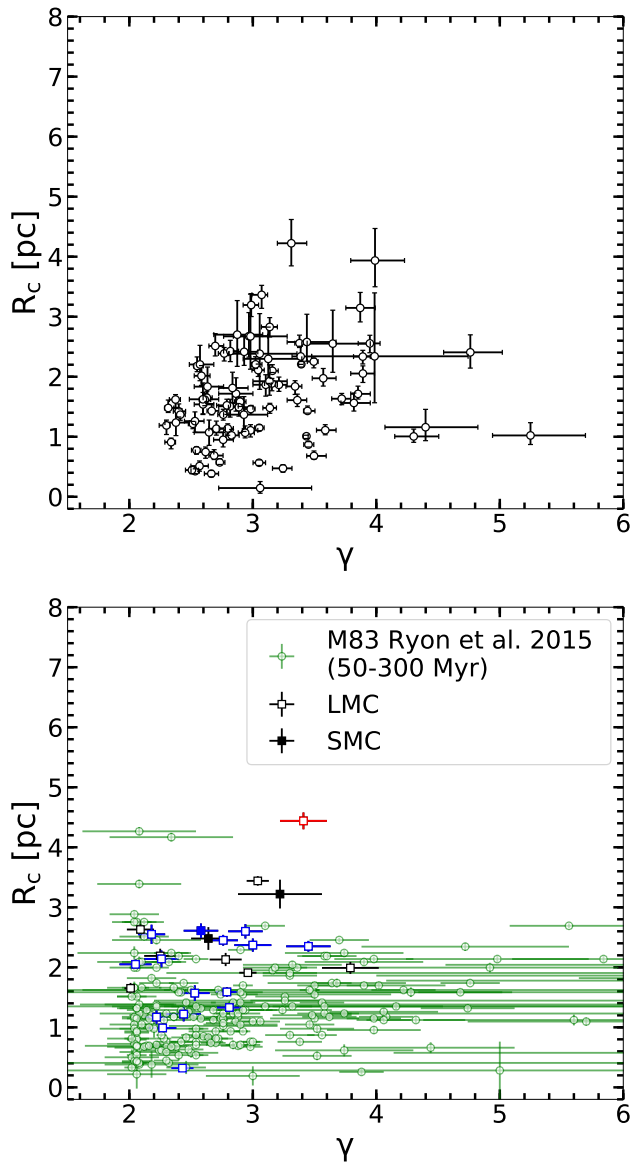


**Figure 16.**  $R_c$  vs  $\gamma$  diagram for the 99 M82 SSCs (top), and the clusters in LMC and SMC from Mackey & Gilmore (2003a,b), as well as M83 from Ryon et al. (2015) (bottom), all fitted with Moffat-EFF profiles. The bars represent the errors in the  $R_c$  vs  $\gamma$  plane. In both the plots, intermediate-age clusters (50–300 Myr) are shown with black symbols, and younger and older clusters are shown with blue and red symbols, respectively. The M83 data is shown in a single colour, since it only corresponds to the intermediate age range (50–300 Myr).

to our log-normal distribution in M82. On the other hand,  $R_c$  distributions in M83 and M82 are comparable, with systematically larger core sizes for M82 SSCs. Detailed analysis of these differences, taking into account cluster masses, ages, host galaxy properties will be addressed in a forthcoming paper.

## ACKNOWLEDGEMENTS

We greatly appreciate the valuable suggestions we received from an anonymous referee, which has improved this manuscript, especially in the presentation of the last 3 figures. BCO thanks CONACyT for granting PhD research fellowship that enabled her to carry out the work presented here. We also thank CONACyT for the research grants CB-A1-S-25070 (YDM), CB-2014-240426 (IP), and CB-A1-S-22784 (DRG), that allowed the acquisition of a cluster that was used for computations in this work. Special thanks to Sergiy Silich for accepting BCO as his research assistant during the later stages of this work.

This paper has been typeset from a  $\text{\TeX}/\text{\LaTeX}$  file prepared by the author.

## REFERENCES

- Avni Y., 1976, *ApJ*, **210**, 642
- Barmby P., McLaughlin D. E., Harris W. E., Harris G. L. H., Forbes D. A., 2007, *AJ*, **133**, 2764
- Bastian N., 2016, *EAS Publications Series*, 80–81, 5
- Bastian N., Goodwin S. P., 2006, *MNRAS*, **369**, L9
- Bastian N., Gieles M., Goodwin S. P., Tranco G., Smith L. J., Konstantopoulos I., Efremov Y., 2008, *MNRAS*, **389**, 223
- Bastian N., et al., 2011, *MNRAS*, **417**, L6
- Baumgardt H., Hilker M., 2018, *MNRAS*, **478**, 1520
- Bertin E., 2011, in Evans I. N., Accomazzi A., Mink D. J., Rots A. H., eds, *Astronomical Society of the Pacific Conference Series Vol. 442, Astronomical Data Analysis Software and Systems XX*. p. 435
- Bertin E., Arnouts S., 1996, *A&AS*, **117**, 393
- Binney J., Tremaine S., 1987, *Galactic dynamics*. Princeton University Press
- Chandar R., Ford H. C., Tsvetanov Z., 2001, *AJ*, **122**, 1330
- Chandar R., Whitmore B. C., Calzetti D., Di Nino D., Kennicutt R. C., Regan M., Schinnerer E., 2011, *ApJ*, **727**, 88
- Davidge T. J., 2008, *AJ*, **136**, 2502
- Djorgovski S., 1995, *ApJ*, **438**, L29
- Elson R. A. W., Fall S. M., Freeman K. C., 1987, *ApJ*, **323**, 54
- Elson R. A. W., Schade D. J., Thomson R. C., Mackay C. D., 1992, *MNRAS*, **258**, 103
- Fall S. M., Zhang Q., 2001, *ApJ*, **561**, 751
- Forbes D. A., et al., 2018, *Proceedings of the Royal Society of London Series A*, **474**, 20170616
- Freedman W. L., et al., 1994, *ApJ*, **427**, 628
- Fujii M. S., Saitoh T. R., Portegies Zwart S. F., 2012, *ApJ*, **753**, 85
- Gieles M., 2013, *Memorie della Societa Astronomica Italiana*, **84**, 148
- Gieles M., Zwart S. F. P., Baumgardt H., Athanassoula E., Lamers H. J. G. L. M., Sipior M., Leenaarts J., 2006, *MNRAS*, **369**, 793
- Jedrzejewski R. I., 1987, *MNRAS*, **226**, 747
- King I., 1962, *AJ*, **67**, 471
- King I. R., 1966, *AJ*, **71**, 64
- Konstantopoulos I. S., Bastian N., Smith L. J., Westmoquette M. S., Tranco G., Gallagher III J. S., 2009, *ApJ*, **701**, 1015
- Kormendy J., 1985, *ApJ*, **295**, 73
- Larsen S. S., 1999, *A&AS*, **139**, 393
- Lynden-Bell D., Wood R., Royal A., 1968, *MNRAS*, **138**, 495
- Mackey A. D., Gilmore G. F., 2003a, *MNRAS*, **338**, 85
- Mackey A. D., Gilmore G. F., 2003b, *MNRAS*, **338**, 120
- Mackey A. D., Wilkinson M. I., Davies M. B., Gilmore G. F., 2008, *MNRAS*, **386**, 65

- Mayya Y. D., Carrasco L., Luna A., 2005, *ApJ*, **628**, L33
- Mayya Y. D., Bressan A., Carrasco L., Hernández-Martínez L., 2006, *ApJ*, **649**, 172
- Mayya Y. D., Romano R., Rodríguez-Merino L. H., Luna A., Carrasco L., Rosa-González D., 2008, *ApJ*, **679**, 404
- McLaughlin D. E., 2000, *ApJ*, **539**, 618
- McLaughlin D. E., van der Marel R. P., 2005, *ApJS*, **161**, 304
- McLaughlin D. E., Barmby P., Harris W. E., Forbes D. A., Harris G. L. H., 2008, *MNRAS*, **384**, 563
- Melo V. P., Muñoz-Tuñón C., Maíz-Apellániz J., Tenorio-Tagle G., 2005, *ApJ*, **619**, 270
- Moreno E., Pichardo B., Velázquez H., 2014, *The Astrophysical Journal*, **793**, 110
- Mutchler M., et al., 2007, *PASP*, **119**, 1
- O’Connell R. W., Gallagher John S. I., Hunter D. A., Colley W. N., 1995, *ApJ*, **446**, L1
- Parker R. J., Wright N. J., Goodwin S. P., Meyer M. R., 2014, *MNRAS*, **438**, 620
- Peng C. Y., Ho L. C., Impey C. D., Rix H.-W., 2010, *AJ*, **139**, 2097
- Portegies Zwart S. F., McMillan S. L. W., Gieles M., 2010, *ARA&A*, **48**, 431
- Press W., Teukolsky S., Vetterling W., Flannery B., 1992, *Numerical Recipes in Fortran 77: The art of Scientific Computing*, 2 edn. Cambridge University Press
- Ryon J. E., et al., 2015, *MNRAS*, **452**, 525
- Ryon J. E., et al., 2017, *ApJ*, **841**, 92
- Santiago-Cortés M., Mayya Y. D., Rosa-González D., 2010, *MNRAS*, **405**, 1293
- Silich S., Tenorio-Tagle G., 2017, *MNRAS*, **465**, 1375
- Sirianni M., et al., 2005, *PASP*, **117**, 1049
- Smith L. J., Gallagher J. S., 2001, *MNRAS*, **326**, 1027
- Sollima A., Baumgardt H., Zocchi A., Balbinot E., Gieles M., Hénault-Brunet V., Varri A. L., 2015, *MNRAS*, **451**, 2185
- Spitzer L. S., 1987, *Dynamical Evolution of Globular Clusters*. Princeton University Press
- Walker D. L., Longmore S. N., Bastian N., Kruijssen J. M. D., Rathborne J. M., Jackson J. M., Foster J. B., Contreras Y., 2015, *MNRAS*, **449**, 715
- Wall J. V., Jenkins C. R., 2003, *Practical statistics for astronomers*. Cambridge Observing Handbooks for Research Astronomers, Cambridge Univ. Press, Leiden
- Wang S., Ma J., 2013, *The Astronomical Journal*, **146**, 20
- Whitmore B. C., Schweizer F., 1995, *AJ*, **109**, 960
- Whitmore B. C., et al., 2016, *AJ*, **151**, 134
- Wilson C. P., 1975, *AJ*, **80**, 175
- Yun M. S., 1999, in Barnes J. E., Sanders D. B., eds, *IAU Symposium Vol. 186, Galaxy Interactions at Low and High Redshift*. p. 81
- de Vaucouleurs G., de Vaucouleurs A., Corwin Herold G. J., Buta R. J., Paturel G., Fouque P., 1991, *Third Reference Catalogue of Bright Galaxies*

## APPENDIX A: ELLIPTICITY DISTRIBUTION OF M82 DISK SSCS

Observed structures of stellar clusters are best described by isothermal models which have intrinsically axially symmetric radial intensity profiles (e.g. King 1966). However, observed clusters are not always spherically symmetric. In such cases, it is a common practice to obtain radial intensity profiles of observed clusters using circularly symmetric isophotes. In this appendix, we discuss the effect of obtaining surface brightness profiles (SBPs) using almost circular isophotes for clusters that may have a non-negligible ellipticity. In Fig. A1, we show the distribution of ellipticity for our sample of 99 SSCs in the disk of M82. These ellipticities are measured at the semi-major axis= $R_{\text{fit}}$  value for

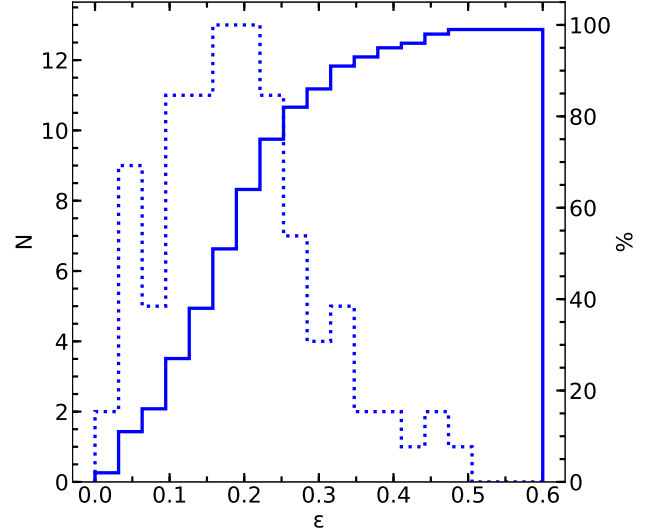


**Figure A1.** Distribution of ellipticities measured using elliptical isophotes of the sample of 99 M82 disk SSCs (dotted line). The cumulative distribution is shown with a solid line.

**Table A1.** Geometrical properties of M82 disk SSCs.

| ID  | $\epsilon$ | P.A. |
|-----|------------|------|
| (1) | (2)        | (3)  |
| D1  | 0.30       | 56   |
| D4  | 0.16       | 5    |
| D7  | 0.41       | 44   |
| D8  | 0.20       | 58   |
| D10 | 0.24       | 53   |
| D14 | 0.23       | -25  |
| D15 | 0.40       | 71   |

Col (1): Numerical ID, taken from Mayya et al. (2008). Col (2): Measured ellipticity. Col (3): Measured position angle in degrees. The full table is shown in the electronic edition; a portion is shown here for guidance.

each cluster in the V-band using the IRAF/STSDAS task *ellipse*. The plotted value corresponds to the average of ellipticities at three consecutive ellipses centered at  $R_{\text{fit}}$ . In the figure, we also show the cumulative distribution of ellipticity. The distribution of ellipticities peaks at 0.19 with only 25% of the SSCs having higher ellipticities. Thus, the majority of the SSCs are nearly circular.

In Figure A2, we illustrate the effect of using almost circular rings ( $\epsilon=0.05$ ) for measuring the SBP of a cluster that has  $\epsilon = 0.30$ . We chose well-known SSC M82-F (D1), one of the most elongated clusters, for illustration. We follow the same procedure as explained in Sec. §3 to fit the profiles using Moffat-EFF model to the SBP obtained from  $\epsilon = 0.30$ . The observed SBPs obtained with  $\epsilon = 0.05$  and  $\epsilon = 0.3$ , along with the respective best-fit models are shown in the figure. The  $r_d$  and  $\gamma$  values for these two SBPs are identical within the errors of the measurements. This illustrates that the derived structural parameters are not very sensitive to small differences in ellipticities. Hence, obtaining SBPs using circular apertures gives equally good values for clusters with  $\epsilon$  as large as  $\sim 0.3$ .



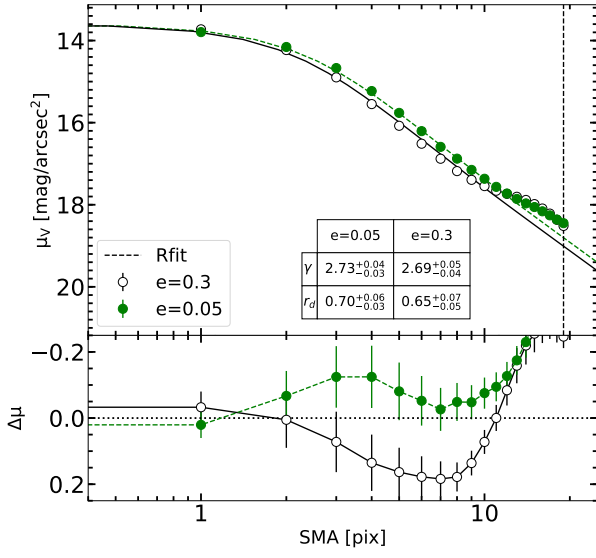


**Figure A2.** Surface brightness profiles for the cluster D1, with nearly circular ( $e=0.05$ ) and with elliptical ( $e=0.3$ ) isophotes (upper panel) and the corresponding residuals (bottom panel).